
Development of a Support-Cathode-Electrolyte Structure for Direct Carbon Fuel Cell

A Thesis

Submitted to

WORCESTER POLYTECHNIC INSTITUTE

In partial fulfillment of the requirements for the

Degree of Master of Science

in

Materials Science and Engineering

by

Steven Jacek

December 2021

Advisor:
Professor Adam Powell

Committee:
Dr. Boyd Davis
Professor Uday Pal
Professor Bilge Yildiz
Professor Yu Zhong

Abstract

Electricity is an increasingly important resource in the world's energy system, but conventional methods of energy production are based on technology which is neither efficient nor sustainable. Fuel cells are a known technology for electricity production, but suffer from poor operating life and manufacturability. A high-energy, high-efficiency direct carbon fuel cell (DCFC) has been proposed by Davis et al. which consists of a liquid metal anode, into which is submerged a tubular cathode-electrolyte structure.

This structure is a three-layer ceramic composite consisting of a coarsely porous support, finely porous cathode, and fully dense electrolyte. Its development is described herein.

The support layer is made of calcium-doped lanthanum manganite (LCM), the cathode active layer from a blend of LCM and yttria-stabilized zirconia (YSZ), and the electrolyte from YSZ. The support is slip cast; the cathode and electrolyte are dip-coated onto the support and dried before sintering.

The support, which also functions as the current collector, is made of LCM and has a porosity of about 35 vol % 20 μ m pores. It is fabricated to a thickness of 2mm by slip casting with a casting time of 5 minutes. The cathode layer is made of an equal mass blend of LCM and YSZ so both its shrinkage upon sintering and thermal expansion coefficient are compatible with those of both the support and the electrolyte, preventing delamination during fabrication or operation. It has a fired porosity of about 35 vol% 5 μ m pores, and a thickness of about 40 μ m. It is applied to the support by dip coating. The electrolyte is made of zirconia doped with 8 mol % yttria to maximize oxygen ion vacancies. It is applied to the structure by dip coating on top of the dried cathode layer and has a thickness of about 20 μ m with closed porosity well below 10 vol%.

The structure is co-fired for 2 hours at 1300°C. It is fired horizontally to maintain even sintering throughout the length.

The structure was tested in conjunction with a molten alloy anode as a complete fuel cell. The cathode-electrolyte structure did not display damage or significant degradation after about 5 hours in contact with the molten anode at about 1000°C. A promising result from electrical testing is that the initial open-circuit voltage nearly reaches the theoretically-predicted value and decreases as the cell operates.

This thesis focuses on the fabrication process of the cathode-supported electrolyte structure. In Chapter 1, context, motivation, and basic theory relevant to the process steps developed are presented. In Chapter 2, similar work is critically examined. Chapter 3 provides details of prototyping and characterization techniques which were used repeatedly in the development process, in the hope that other researchers may replicate and improve upon them. The development process itself is described in Chapter 4; discussion of design decisions and possible alternatives is here as well. Chapters 5 and 6 summarize the most valuable outcomes of this work, and Chapter 7 suggests strategies for improving this technology in future work.

Learnings from this work will contribute to the technical literature, particularly in the areas of formulation and processing, advancing the future of DCFC technology.

Acknowledgements

I would first like to thank my advisor, Adam Powell, for the opportunity to pursue this research under his guidance. I appreciate his flexibility to work with me as a part-time student balancing responsibilities. The entire Energy Metals Research Group, especially Aditya Moudgal, Gabriel Espinosa, Alexander Wadsworth, and Mahya Shahabi for their help with cell testing, deserve thanks. I likewise extend thanks to Jack Grubbs and the entire Cote Research Team for their assistance in the lab, Shelly Woods for always-timely purchasing support, and Mike Collins for providing training on lab equipment.

For their time and input, I would also like to extend thanks to my thesis committee: Boyd Davis, Uday Pal, Yu Zhong, and Bilge Yildiz.

Thank you to Kyung Joong Yoon at The Korea Institute of Science and Technology for his helpful technical consultation.

Sincere thanks to Boyd Davis, Trevor Lebel, and Spencer Jeffrey at Kingston Process Metallurgy for preparing the anode alloys for this work.

I would like to thank my employer, Saint-Gobain, for financial support towards my Master's degree, for cultivating a culture which encourages and enables higher education, and for providing access to formulation and characterization facilities integral to this work. Thank you to Jeff Peet, Subramanian Ramalingam, and Nicolas Drolet for their flexibility in my schedule over several years. Thank you to my colleagues Courtland Chapman, Ray Dube, Colleen McDowell, and Chad Bleakney for their helpful input.

Thank you to my parents, Vic and Rae Ann Jacek, for instilling in me an unending curiosity about the world around me and the value of lifelong learning. Thank you to my brothers Victor and Nicholas Jacek for exploring the world with me and blazing paths for me in education and achievement.

Finally and most importantly, thank you to my wife Jenna for her unwavering support and encouragement, logistical and emotional. Thank you for deepening my purpose in this and all things.

Contents

1	Introduction	1
1.1	Motivation	1
1.2	Fuel cells	1
1.2.1	<i>Direct carbon fuel cells</i>	1
1.2.2	<i>High efficiency, high power density DCFC design</i>	4
1.3	Ceramic processing	8
1.3.1	<i>Powder characterization by zeta potential</i>	8
1.3.2	<i>Slip casting</i>	10
1.3.3	<i>Dip coating</i>	11
1.3.4	<i>Sintering</i>	12
2	Related works	13
3	Methodology	15
3.1	Slurry preparation	15
3.2	Zeta potential characterization	16
3.3	Rheology characterization	16
3.4	Slip casting	16
3.5	Porosity characterization by Archimedes method	17
3.6	Dip coating of cathode and electrolyte	18
3.7	Firing	19
3.8	SEM imaging	21
3.9	Cell testing	21
3.9.1	<i>Alloy preparation</i>	21
3.9.2	<i>Apparatus description and preparation</i>	22
3.9.3	<i>Apparatus operation and measurement</i>	25
4	Development	25
4.1	Fabrication process overview	25
4.2	Active material choice	26
4.3	Formulation	27
4.3.1	<i>Powder characterization by zeta potential</i>	27
4.3.2	<i>LCM support/current collector formulation</i>	30
4.3.3	<i>LCM/YSZ cathode</i>	37
4.3.4	<i>YSZ electrolyte</i>	40
4.4	Dip coating of cathode and electrolyte	45
4.5	Firing	47
4.6	Scale-up	49
5	Results	51
5.1	Composite characterization by SEM	51
5.2	Cell testing	55
5.2.1	<i>Mechanical and Thermal</i>	55
5.2.2	<i>Electrical</i>	58
6	Conclusions	59

7	Future Work	60
8	References	61

List of Figures

Figure 1.1: The major components of a fuel cell. (Giddey et al., 2012).	2
Figure 1.2: Conceptual schematic of the DCFC which the present work develops.	5
Figure 1.3: Schematic of the cross-section of the support-cathode-electrolyte structure of the proposed DCFC.	6
Figure 1.4: Visual explanation of how doping zirconia with yttria creates oxygen ion vacancies in the resulting structure. The vacancies allow oxygen ion transport.	7
Figure 1.5: Schematic of a colloidal particle submerged in an electrolyte-containing liquid. The electrical charge at the slipping plane is the zeta potential, which is an important parameter in slurry formulation.	9
Figure 1.6: The slip casting process. a) The gypsum mold. b) The mold filled with slip during casting. c) The cast in the drained mold. d) The trimmed green cast. (Reed, 1995).	10
Figure 1.7: The form of the relationship between relative viscosity of a slurry and its solids content. (Reed, 1995).	11
Figure 3.1: Initial setup for creating slip casting molds. The plaster was poured around the suspended rod, and once dry, the rod was removed.	16
Figure 3.2: Hemispherical-bottomed mold, and the ball-end router tool used to create it.	17
Figure 3.3: A dry support which has just been dip coated with cathode slurry.	18
Figure 3.4: Dip-coated samples resting in their holders. Left: a dry cathode coating. Right: a dry electrolyte coating.	19
Figure 3.5: Firing trays used to lay-fire samples.	19
Figure 3.6: Firing curve #1. This curve is used when the sample being fired is an LCM support.	20
Figure 3.7: Firing curve #2. This curve is used for sintering samples which include a cathode layer. (Yoon, 2008).	20
Figure 3.8: Setup used to melt the anode alloy.	22
Figure 3.9: High-temperature electrochemistry apparatus, from Faria (2021).	23
Figure 3.10: Testing insert for which was used to suspend the anode-containing crucible, cathode-electrolyte structure, and graphite fuel rod in the furnace.	24
Figure 3.11: The Mellen induction furnace used to test the cell. The testing insert is inserted into the hole. The testing insert's flange is supported by the flange of the furnace tube.	25
Figure 4.1: The generalized process followed to fabricate cathode-electrolyte structure prototypes.	26
Figure 4.2: Zeta potential of LCM over a range of pH.	27

Figure 4.3: Zeta potential of LCM in DI water as concentration of Dolapix CE-64 is increased.....	28
Figure 4.4: pH-corrected ZP of LCM with Dolapix CE-64 dispersant. A ZP of ± 40 mV is considered to give good dispersion stability (Kumar and Dixit, 2017).	28
Figure 4.5: Zeta potential of YSZ in DI water as a function of pH.....	29
Figure 4.6: Zeta potential and pH of YSZ in DI water as Dolapix CE-64 concentration is increased. .	29
Figure 4.7: pH-corrected ZP of YSZ with Dolapix CE-64 dispersant. A ZP of ± 40 mV is considered to give good dispersion stability (Kumar and Dixit, 2017).	30
Figure 4.8: Casted supports with varying levels of PVA binder. Note that these samples were made with LSM rather than LCM and did not contain pore former.....	31
Figure 4.9: The taper of the walls in 3 support casts vs the binder content. The taper is calculated as the wall thickness at the top minus the wall thickness at the bottom, all divided by the height of the part. Note that these parts were made of LSM instead of LCM.....	32
Figure 4.10: Rheology of LSM samples with various binder amounts. Tested with 2° cone and plate geometry.....	32
Figure 4.11: Porosity of LCM support after 1, 2, and 3 firing cycles of Curve #1.....	33
Figure 4.12: An LCM support sample which has cracked in the mold.....	34
Figure 4.13: Porosity of LCM samples formulated to 77 dry volume % cellulose after various firing cycles of firing Curve #1.	34
Figure 4.14: Viscosity of LCM slurry formulated to 77 dry volume % pore former and low binder content compared to a slurry formulated with a high binder content but no pore former.	35
Figure 4.15: LCM casts with various binder to LCM ratios. All samples were formulated to 77 dry volume % cellulose pore former.....	36
Figure 4.16: Cast supports which have been formulated to various porosities. The sample containing 50 dry volume % pore former was the only one which did not crack in the mold.	36
Figure 4.17: Formulated and fired porosity of samples made with various formulations.....	37
Figure 4.18: Fired and formulated porosity of cathode samples using two different grades of carbon black.....	39
Figure 4.19: Left: the setup used to tape cast the YSZ slurry. Right: The dried YSZ film. This technique was a failed attempt to characterize the porosity of the electrolyte layer without coating it on a complete cell, but was not used in fabrication of the titular structure.	41
Figure 4.20: SEM micrograph showing the thickness of the electrolyte at this point in development to be about 40 μ m.....	42
Figure 4.21: SEM micrograph showing almost full density of the YSZ electrolyte layer.....	42

Figure 4.22: Rheology of YSZ slurries at various solids loadings. As expected, higher solids loading corresponds to higher viscosity.	43
Figure 4.23: SEM micrograph showing the thickness of the electrolyte layer to be about 30 μ m. Cracks are present because the firing process had yet to be fully developed.....	44
Figure 4.24: SEM micrograph showing the thickness of the electrolyte layer to be about 40 μ m. Cracks are present because the firing process had yet to be fully developed.....	45
Figure 4.25: An unfired LCM support sample being dip coated. The sample is hung from a holder and the coating bath is raised around it. This method was problematic.	46
Figure 4.26: The improved dip coating process: the LCM support is dried, then dipped and dried by its flange.	46
Figure 4.27: Firing method possibilities. Method 4 was selected because it produced prototypes without cracks in any layer and is the simplest to implement in manufacturing.....	47
Figure 4.28: The result of firing methods 1 and 3. Left: A cathode layer which has cracked during firing. Right: the inside view of the same sample, showing a support with no significant cracking...	48
Figure 4.29: The result of firing method 2. Left: an electrolyte layer which has cracked during firing. Right: the inside view of the same sample, showing a support with no significant cracking.....	48
Figure 4.30: Left: an uncracked electrolyte layer. Pinhole defects in the electrolyte are due to entrained air in the slurry. This is the result of firing method 4. Right: the inside of the same sample, showing no cracks in the support.....	49
Figure 4.31: Mandrel used for producing scaled-up plaster molds. The mandrel was inserted into wet plaster and removed when the plaster dried.....	50
Figure 4.32: Three-part case mold and plaster mold produced with it.....	50
Figure 4.33: Samples casted in the scaled-up mold. They cracked while drying in the mold.	51
Figure 5.1: SEM images of Cell 1. a) Low-magnification view showing all 3 layers and thickness of support. b) View showing all 3 layers distinctly, and thicknesses of cathode and electrolyte. c) High-magnification view showing low porosity in electrolyte. d) High-magnification view showing porosity in the cathode. e) High-magnification view showing porosity in the support.....	53
Figure 5.2: SEM images of Cell 3. a) Low-magnification view showing all 3 layers and thickness of support. b) View showing all 3 layers distinctly, and thicknesses of cathode and electrolyte. c) High-magnification view showing lack of porosity in electrolyte. d) High-magnification view showing porosity in the cathode. e) High-magnification view showing porosity in the support.....	53
Figure 5.3: SEM images of Cell 6. a) Low-magnification view showing all 3 layers and thickness of support. b) View showing all 3 layers distinctly, and thicknesses of cathode and electrolyte. c) High-magnification view showing lack of porosity in electrolyte. d) High-magnification view showing porosity in the cathode. e) High-magnification view showing porosity in the support.....	54

Figure 5.4: Left: Schematic of the intended structure of the support-cathode-electrolyte structure. Right: SEM image of the produced structure.	54
Figure 5.5: Left: cathode-electrolyte structure before testing. Right: The same structure after testing.....	55
Figure 5.6: SEM cross-sections of a cathode-electrolyte structure which was operated at 1000°C for about 1.5 hours. a) The total thickness of the structure. b) The electrolyte-cathode and cathode-support interfaces. c) The outer edge of the electrolyte. d) The electrolyte-cathode interface. e) The cathode-support interface.	56
Figure 5.7: SEM cross-sections of a cathode-electrolyte structure which was operated at 1000°C-1100°C for about 5 hours. a) The total thickness of the structure. b) The electrolyte-cathode and cathode-support interfaces. c) The outer edge of the electrolyte. d) The electrolyte-cathode interface. e) The cathode-support interface.....	57
Figure 5.8: Alloy 1 post-testing. Complete melting was achieved.....	58
Figure 5.9: The anode current collector post-testing.....	58
Figure 5.10: OCV measurements over 30 minutes of operation at 1000C.	59

List of Tables

Table 1.1: Alloys identified by Faria in 2021 as promising for use in this DCFC.	6
Table 1.2: Stability behavior of dispersions as a function of zeta potential (Kumar and Dixit, 2017). 9	
Table 1.3: Summary of mass transport mechanisms relevant to solid state sintering. Adapted from Reed, 1995.....	13
Table 2.1: Summary of relevant design choices of related works.....	14
Table 4.1: General formulation of the LCM support.....	30
Table 4.2: The final formulation for the LCM support.....	37
Table 4.3: The initial formulation for the cathode slurry.	38
Table 4.4: Formulation for the cathode slurry using Regal 250R carbon black.....	38
Table 4.5: Final cathode slurry formulation.....	40
Table 4.6: General formulation of the YSZ electrolyte slurry.....	40
Table 4.7: Formulation used for tape-casting the electrolyte slurry.	41
Table 4.8: Final formulation for the YSZ electrolyte slurry.	45
Table 5.1: Summary of samples characterized by SEM cross-section.....	52

List of abbreviations

Term	Abbreviation
Activated carbon	AC
Atmospheric plasma spray	APS
De-ionized	DI
Electrochemical vapor deposition	EVD
Gadolinium-doped ceria	GDC
Lanthanum Calcium Manganite	LCM
Lanthanum strontium cobalt ferrite	LCSF
Lanthanum Manganite	LMO
Lanthanum Strontium Manganite	LSM
Open circuit voltage	OCV
Polyvinyl alcohol	PVA
Polyvinyl chloride	PVC
Scanning electron microscope	SEM
Solid oxide fuel cell	SOFC
Scandia-stabilized Zirconia	SSZ
United States	US
Volume	vol
Weight	wt
Yttria-stabilized Zirconia	YSZ
Zeta Potential	ZP

1 Introduction

1.1 Motivation

Eighty-seven percent of the world's population has reliable access to electricity (Ritchie and Roser, 2020), which has increased from 71% in 1990. For those of us with access, electrical power has become a necessity. Indeed, forecasts out to the year 2060 expect that electricity will play an increasingly important role in the world's energy system, regardless of geography and energy policy (Kober et al., 2020).

In parallel, global warming due to increased greenhouse gas emissions continues to be a looming threat (Florides and Christodoulides, 2009). Preventing a global temperature increase of more than 2°C, which is the goal of the Paris Accord, "remains an enormous challenge" (Kober et al., 2020).

Yet, according to a 2014 study by the International Panel on Climate Change (IPCC), 25% of the world's greenhouse gas emissions are from electricity production and heat generation. (IPCC, 2014.) The US alone emitted over 1,600 million metric tons of CO₂ in 2019 from electricity generation alone (EPA, 2019). In 2020, coal and natural gas power plants accounted for 99% of these emissions (EPA, 2019), even though they produce only 62% of the nation's electricity (EIA, 2020).

Clearly, if humanity's growing electricity requirement is to be met without severe environmental consequences, innovation is required in this field. A comprehensive 2020 study by Kober et al. identified increased energy efficiency and carbon capture as two of the three most important areas of focus for such innovation.

The present work is towards a technology which has the potential to contribute to both of these focus areas.

1.2 Fuel cells

1.2.1 *Direct carbon fuel cells*

An electrochemical cell is a device which can convert between electrical and chemical potential energy. The working principle of an electrochemical cell is the reduction-oxidation reaction. Electrochemical cells consist of a cathode, where the reduction half-reaction takes place, an anode, where the oxidation half-reaction takes place, and an electrolyte. The electrolyte separates the cathode and the anode, is electrically insulating, and ionically conductive.

Cells designed to run "forward" consume electrical energy to perform a non-spontaneous chemical reduction reaction. Such cells are commonly used to perform electrolysis reactions, and so are called electrolytic cells. An important example of industrial use of electrolytic cell technology is the decomposition of bauxite, a mined mineral, to aluminum metal, which is critical to countless manufacturing processes.

Cells designed to run “backward” consume a fuel which undergoes a non-combustion oxidation reaction to produce electricity. Such devices are termed fuel cells. A basic representation of a fuel cell is given in Figure 1.1.

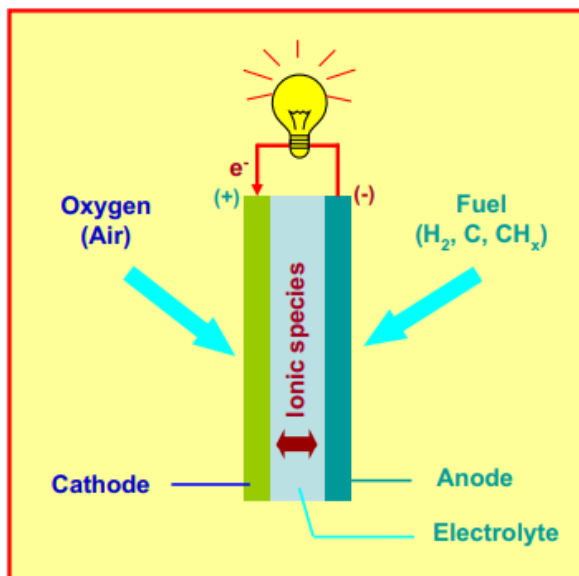


Figure 1.1: The major components of a fuel cell. (Giddey et al., 2012).

Types of fuel cells are commonly named by their fuel or electrolyte material. Many are familiar with hydrogen fuel cells which are currently used to generate power in cars, houses, and portable power units (U.S. Department of Energy). Direct carbon fuel cells (DCFCs) are so termed because they use carbon as a fuel and convert it directly to electrical energy without converting it to a gas, as in combustion (Giddey et al., 2012). This distinction is somewhat redundant but serves to emphasize the fact that the energy comes directly from a chemical reaction, without involving efficiency-lowering concepts such as state changes and moving parts, which are integral in gas turbines. Indeed, the theoretical efficiency of a DCFC using solid fuel is 100%, and projected practical efficiencies are near 80% (Giddey et al., 2012). Modern power plants based on gas turbine technology have practical efficiencies of up to about 60%.

The high theoretical efficiency of the DCFC is in part a result of the low change in entropy of its working reaction,



which has a standard entropy change of $-0.094 \frac{kJ}{mol \cdot K}$.

The anodic and cathodic half-reactions, respectively, are



and



Ideally, all the carbon in the fuel would form CO_2 . In practice, since the cell will operate above $750^\circ C$, some carbon will form carbon monoxide (Wagman, 1945) by the reaction



which will decrease the efficiency of the cell. The proportion of CO_2 to CO evolved in the cell will be equal to the ratio of partial pressure of oxygen feed to the partial pressure of the exhaust gas, which is a function of cell operating temperature (Faria, 2021).

Among cathode-supported DCFCs, two popular geometries exist: planar and tubular. The major advantage of the tubular design is the ease with which the oxidant gas and exhaust gas can be segregated. Planar cell geometries struggle to provide adequate seals between the two (Giddey et al., 2012).

One popular performance metric of a fuel cell is its power density, typically measured in Watts per square centimeter. The wattage is the output of the cell, and the area is the surface area of the anode or cathode in contact with the electrolyte. This parameter is important because it gives information not only about the maximum power output, but about the feasibility of the design as well. Infinitely large devices suffer from poor manufacturability.

Another important performance characteristic of a fuel cell is its open circuit voltage (OCV), which represents the total measured potential difference between the anode and the cathode. Comparing the measured OCV to the theoretical total cell potential E_{th} gives insight into the cell's performance.

To calculate E_{th} , enthalpy, H , and entropy, S , of each relevant species is determined, and then the change in free energy ΔG for reactions (1.1) and (1.4) is determined by

$$\Delta G = \Delta H - T\Delta S \quad (1.5)$$

where T is the temperature, and changes in each value represent the corresponding values for the product side of the reaction minus those on the reactant side. The present work builds on the 2021 work of Faria, who completed these calculations for the relevant species and temperatures, and who determined the relevant enthalpies, entropies, and free energies by the Shomate equation.

At standard temperature and pressure, change in free energy and electromotive force are related by

$$\Delta G = -nFE \quad (1.6)$$

where n is the number of electrons involved in the reaction, F is Faraday's constant, and E is electromotive force in Volts.

If the right-hand side of Equation (1.6) is used in place of ΔG in the overall change in free energy for the cell,

$$\Delta G = \Delta G^0 + RT \ln(Q), \quad (1.7)$$

where Q is the previously described ratio of partial pressures of gasses, then terms can be rearranged to isolate the theoretical cell voltage:

$$E_{th} = E_0 - \frac{RT}{nF} \ln(Q). \quad (1.8)$$

It is important to note that at constant temperature and pressure, the free energy of a particular species is equal to its chemical potential, μ . The chemical potential, in turn, is related to the activity of the species by

$$\mu = \mu^0 + RT \ln(a) \quad (1.9)$$

Where μ^0 is the standard chemical potential of the species, R is the universal gas constant, T is the temperature, and a is the activity of the species. Activity of a species typically varies linearly with its concentration. Since E_{th} depends on E^0 , which in turn depends on free energy which is equal to chemical potential, which depends on activity, it is clear that the voltage of a cell will depend on the activity of the species participating in its working reaction.

Performance characterization of the present work relies on relating changes in measured OCV to changes in the activity of carbon near the electrolyte, and is discussed in Section 5.2.2.

1.2.2 High efficiency, high power density DCFC design

The present work develops the cathode-electrolyte structure of a novel DCFC which has been ideated by Boyd Davis, Adam Powell, and Uday Pal, and upon which Christian Faria began development.

The proposed cell consists of a liquid metal anode into which is submerged a tubular support-cathode-electrolyte structure, which is the focus of the present work. A schematic of the proposed cell is given in Figure 1.2. A schematic of the support-cathode-electrolyte structure's cross-section is given in Figure 1.3 and is helpful in following the working principle of the design, which is as follows:

Oxygen gas (likely in the form of air) is injected into the tubular support-cathode-electrolyte structure. A pressure gradient drives the oxygen through the highly porous support and into the porosity of the cathode. There, it is ionized to form O^{2-} . The oxygen ions are conducted by ionic diffusion through the oxygen ion vacancies in the yttria-stabilized zirconia (YSZ) in the cathode and

in the fully dense YSZ electrolyte. When the oxygen ions reach the electrolyte/anode interface, they participate in an oxidation reaction with the carbon dissolved in the liquid anode. This reaction produces free electrons, which are collected from the anode to perform electrical work. CO₂ is also produced in a nearly pure stream, so it may be easily captured for industrial use or sequestration.

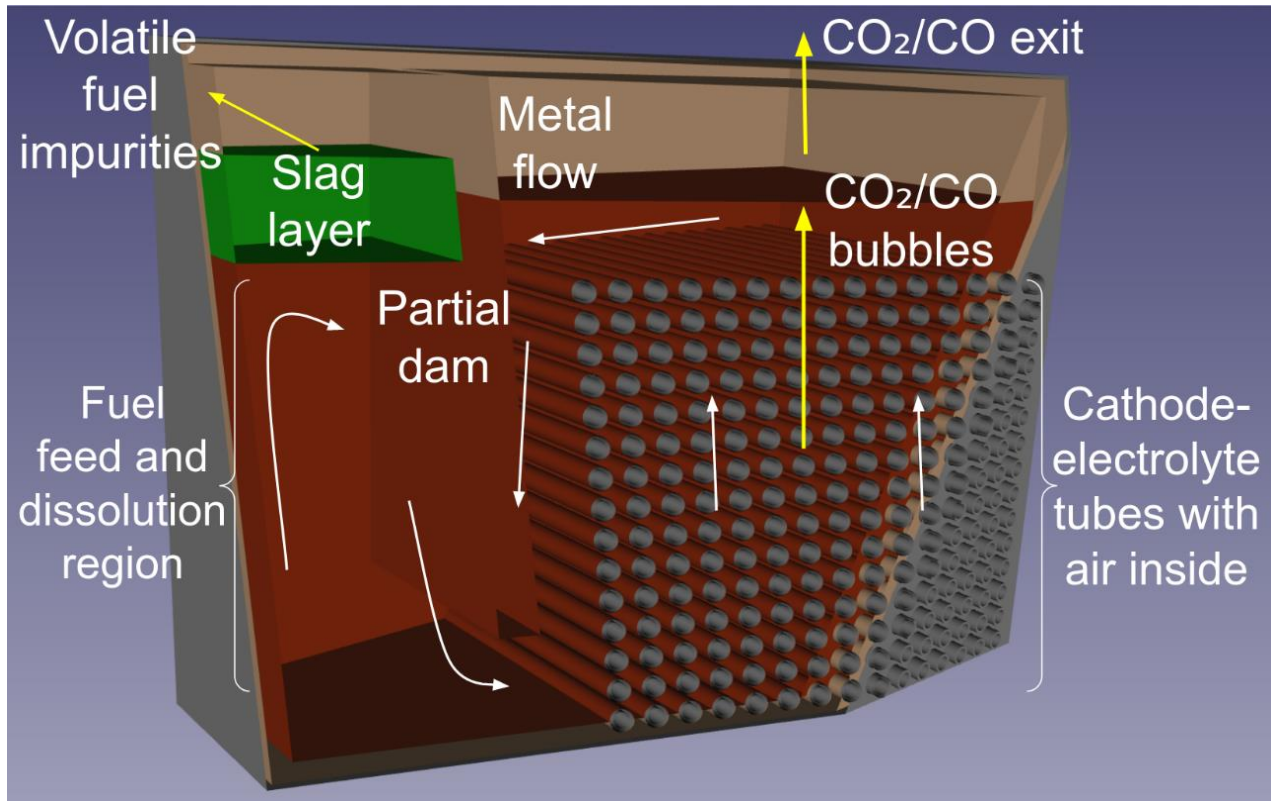


Figure 1.2: Conceptual schematic of the DCFC which the present work develops.

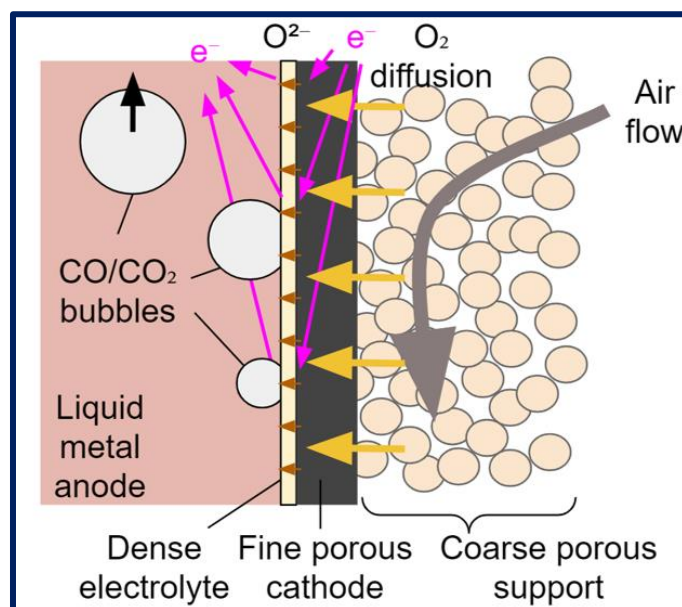


Figure 1.3: Schematic of the cross-section of the support-cathode-electrolyte structure of the proposed DCFC.

The anode technology borrows from steelmaking technology by using alloying elements to increase its carbon solubility and lower its liquidus temperature, thereby lowering the operating temperature of the cell (Faria, 2021). Four promising alloys were identified by Faria, which are detailed in Table 1.1.

Table 1.1: Alloys identified by Faria in 2021 as promising for use in this DCFC.

	Alloy 1	Alloy 2	Alloy 3	Alloy 4
Fe	37.5%	40.0%	66.0%	12.9%
Mn	30.0%	30.0%	10.0%	76.0%
Sn	30.0%	-	-	-
C	2.5%	4.0%	4.0%	1.1%
Ni	-	26.0%	-	-
Mo	-	-	20.0%	-
Si	-	-	-	10.0%

The carbon fuel is supplied to the anode in solid form and migrates to the electrolyte/anode interface as a result of diffusion combined with bubble-stirring. Since CO₂ is produced by the anodic reaction, the geometry of the cell could be designed to make use of the bubbles to agitate the liquid anode and disperse the fuel. Possible fuels include biomass, municipal solid waste, coal, and petcoke. Potentially low fuel purity is addressed by the partial dam between the fuel feed compartment and operation compartment, shown in Figure 1.2. Impurities which are less dense than the anode alloy would float and could be harvested from the fuel feed compartment as a slag layer.

The mechanism for oxygen ion transport through the electrolyte is diffusion through oxygen ion vacancies, which are present in the YSZ due to doping the zirconia structure with yttria. As described by Figure 1.4, doping zirconia with yttria induces oxygen vacancies in the resulting structure, which is termed Yttria-Stabilized Zirconia (YSZ). The vacancies are necessary to charge-balance the structure after substituting Y⁺³ ions in place of Zr⁺⁴ ions.

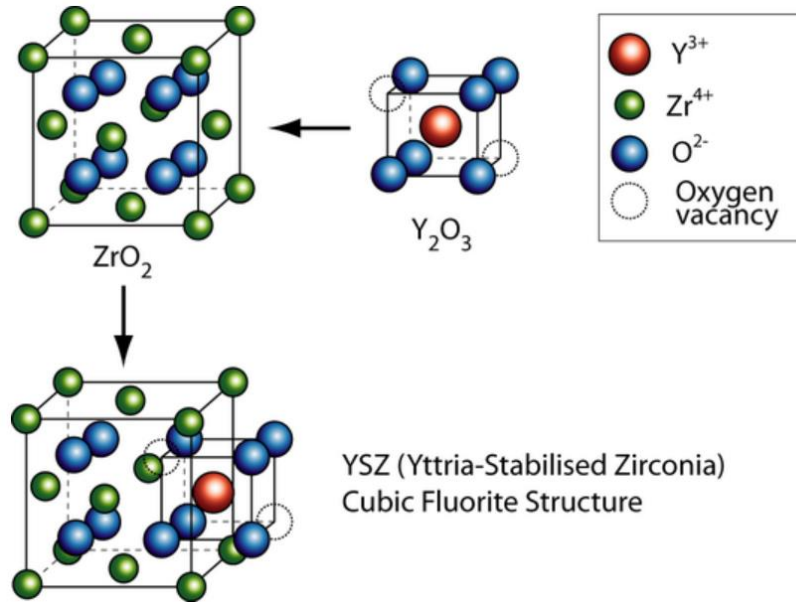


Figure 1.4: Visual explanation of how doping zirconia with yttria creates oxygen ion vacancies in the resulting structure. The vacancies allow oxygen ion transport.

The porosity of the support and the cathode are critical to the cell's performance: without open porosity in these structures, oxygen cannot reach the cathode to be ionized. To allow power scalability by adjusting oxygen flow rate, the present work aims to maximize the porosity in both of these structures so that oxygen delivery to the cathode does not become the limiting factor in power density. As shown in Figure 1.3, large pores, as opposed to more smaller pores, are desired in the support. This is to minimize the pressure loss (thereby maximizing the delivery rate) of the gas as it flows through the porous support into the cathode. Modelling the pores as tubes of approximately circular cross-section, the head loss of the air flowing through them is given by the Darcy-Weisbach equation

$$h = f \frac{LU^2}{2Dg} \quad (1.10)$$

where h is the head loss, f is the friction factor, L is the pipe length, U is the average fluid velocity, D is the pipe diameter, and g is acceleration due to gravity. Pressure loss, P , is then given by

$$P = \rho gh \quad (1.11)$$

Where ρ is fluid density, g is acceleration due to gravity, and h is head calculated by Equation (1.10). Since pressure is the driving force for oxygen delivery, we wish to maximize the pipe diameter D , in order to minimize the head loss h , thereby minimizing the pressure loss P . For this reason, we select atypical pore formers for the support because they can provide larger pore diameters (see Section 4.3.2.)

1.3 Ceramic processing

1.3.1 Powder characterization by zeta potential

For successful application of the ceramic processing techniques chosen for this work, stable and well-dispersed slurries are critical. Ensuring stability and dispersion can be more challenging in aqueous systems than those which use organic solvent, so special attention is given to the topic here.

When a solid particle is submerged in an electrolyte-containing liquid, an electrical double layer forms around the particle (Grahame, 1947). The first layer, called the Stern layer, is formed from ions in the liquid of opposite charge to the particle. The second layer is formed primarily from ions with charge opposite to the particle, but partially from ions with the same charge as the particle, because they are attracted to the ions in the Stern layer. These two layers of particles remain electrostatically adhered to the particle as it travels through the bulk fluid. The slipping plane is defined as the plane at which ions closer to the particle remain adhered to it as it moves through the bulk, and at which ions further from the particle do not adhere strongly enough to travel with the particle.

The zeta potential (ZP) of a system, described by Figure 1.5, is a measure of the electric charge at the slipping plane. It is a function of the particle's surface chemistry, the liquid's chemistry, and the pH of the system. It can be dramatically altered by introducing surfactants to the system. Surfactants are typically highly-charged ionic species which adsorb to the surface of the particle to modify its ZP.

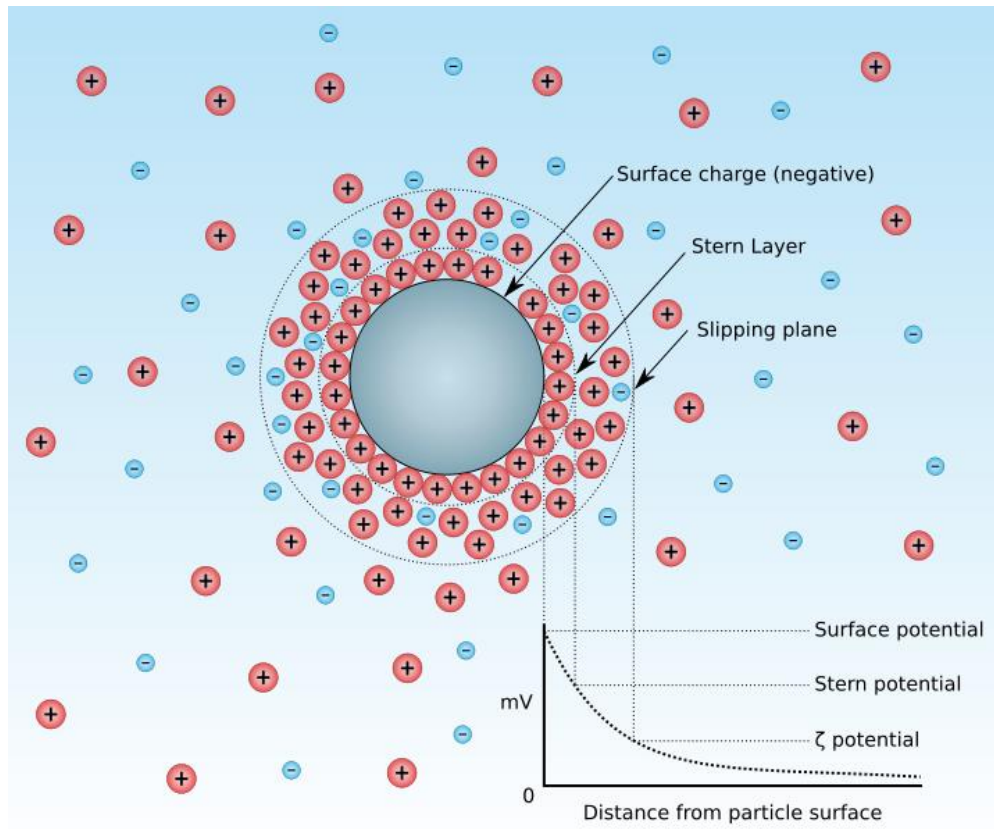


Figure 1.5: Schematic of a colloidal particle submerged in an electrolyte-containing liquid. The electrical charge at the slipping plane is the zeta potential, which is an important parameter in slurry formulation.

Zeta potential is an important consideration in ceramic slurry formulation because in most cases, it is desirable to avoid agglomeration of particles, which can lead to processing issues and microstructural defects in the ceramic part. Incorporating a surfactant which provides a zeta potential of great enough magnitude is a common strategy for preventing agglomeration, because it ensures that there will be sufficient electrostatic repulsion between the dispersed particles. Table 1.2 shows the typical stability behavior of dispersions as a function of zeta potential. For this work, a ZP of $\pm 40\text{mV}$ was targeted for each of the ceramic slurries prepared.

Table 1.2: Stability behavior of dispersions as a function of zeta potential (Kumar and Dixit, 2017).

Zeta potential (mV)	Stability behavior
0 to ± 5	Rapid coagulation or flocculation
± 10 to ± 30	Incipient instability
± 30 to ± 40	Moderate stability
± 40 to ± 60	Good stability
> 61	Excellent stability

1.3.2 Slip casting

A colloidal dispersion of ceramic particles in a solvent, typically water, is called a slip. (More properly, the term “slip” refers specifically to an aqueous dispersion containing clay, but in the field of technical ceramics, it is often used to describe any ceramic dispersion which will be drain-casted. The terms slip casting and drain casting are used interchangeably.) In slip casting, a gypsum mold cavity is filled with slip for a period of time during which casting takes place. During casting, the capillary pressure from the fine pores in the gypsum mold draws water out of the slip and causes the dispersed ceramic particles to compact against the internal walls of the mold cavity. The compacted ceramic layer is called the cast. The mold cavity is refilled with fresh slip as liquid is drawn into the mold and the liquid level decreases. Casting ends when the slip is drained from the mold, typically by inverting the mold, and the wet cast is left behind. The cast continues to dry until it has attained structural integrity and may be removed from the mold. At this point the cast may be referred to as a “green” part, indicating that it has not been sintered. The green part may be trimmed before firing. An overview of the process is given in Figure 1.6 (Reed, 1995).

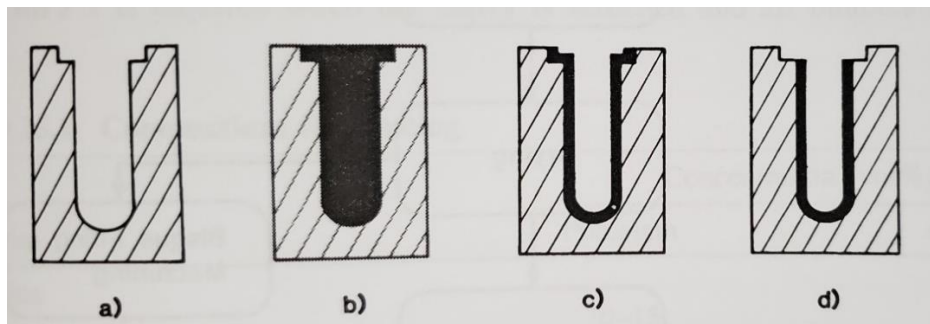


Figure 1.6: The slip casting process. a) The gypsum mold. b) The mold filled with slip during casting. c) The cast in the drained mold. d) The trimmed green cast. (Reed, 1995).

Formulation parameters which affect the final quality of the slip-casted part include slip rheology, solids content, and degree of particle agglomeration.

In terms of rheology, low-shear-rate viscosity and thixotropy are of principal interest. Viscosity is most relevant at low shear rates because it must be high enough to prevent slumping of the wet cast and, preferably, settling of the slurry, both of which are low-shear-rate processes. It must be low enough to allow good draining of the mold once the casting time has elapsed, which also is a low-shear process. A typical slip is slightly thixotropic, meaning its viscosity decreases slightly over time under constant shear. It is desirable that thixotropic effects are strong enough to avoid long casting times and weak enough to avoid long drying times (Reed, 1995).

Increasing the solids content of the slurry increases its viscosity according to the relationship in Figure 1.7 (Reed, 1995). The relative viscosity is the ratio of the slurry viscosity to the viscosity of the solvent with no dispersed particles, and f_{er}^v is the solids loading at which flow is blocked.

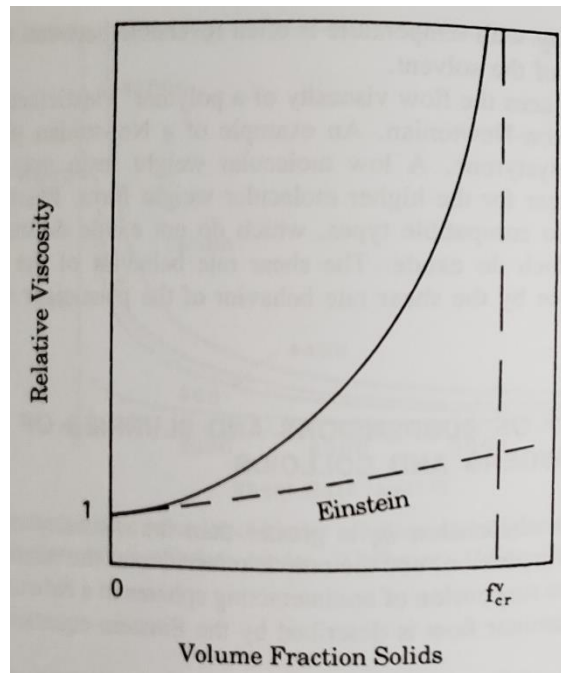


Figure 1.7: The form of the relationship between relative viscosity of a slurry and its solids content. (Reed, 1995).

In addition, increasing the solids content increases casting rate because less liquid must be removed from the slurry to create a packed bed of particles.

Degree of particle agglomeration is a critical formulation parameter in slip casting. A well-dispersed slurry will give a hard, dense cast, while an agglomerated slurry will give a relatively soft, porous cast. For technical ceramics, a fully dispersed slurry is often desired, so that good green strength is achieved and any porosity is intentionally added and controlled.

The primary process parameter which affects the slip-casted part is casting time. A longer casting time results in a thicker cast, and thicker cast will have higher green strength.

A casted part must have sufficient green strength so that it can be handled; in the case of the present work: moved to and from an oven for drying, dip coated, and then lay-fired.

1.3.3 Dip coating

In a dip coating process, a substrate is withdrawn from a coating bath leaving a wet film coated upon the substrate. Typically, the thickness of the coating will be of interest because it determines in some way the performance of the coating. In the case of the present work, the cathode and anode layers of the titular structure are dip coated. They must be thick enough to provide structural integrity, but as thin as possible to maximize oxygen ion transport to the anode.

The thickness of the wet film is determined by a balance of three forces: the viscous forces within the liquid, the surface tension between the liquid and the air, and gravity (Landau and Levich, 1942). This relationship can be described by the dimensionless capillary number

$$Ca = \frac{\eta V}{\gamma} \quad (1.12)$$

where η is the viscosity of the liquid, V is the velocity at which the substrate is withdrawn from the coating bath, and γ is the surface tension between the liquid and the air. In the present work, a relatively small part is being withdrawn from a bath by hand, so V and therefore Ca are small. In this case, the thickness of the wet film can be modeled with only the viscosity and surface tension of the liquid (Gans et al., 2019). Since both of these are formulation parameters, formulation of the cathode and electrolyte slurries is extensively addressed in Section 4.3.

While dip coating theory predicts the wet film thickness, the dry film thickness t_d , ultimately dictates performance and is given by

$$t_d = t_w f_v \quad (1.13)$$

where t_w is the wet film thickness and f_v is the volume fraction of solids in the coating.

In a successful dip coating process, when the substrate is withdrawn from the bath, the liquid does not de-wet from the substrate because the viscous and surface tension forces are in balance. Further, the liquid does not run off of the substrate because the viscous and gravitational forces are in balance. Finally, the coating is of the desired thickness and does not contain defects such as pinholes, streaks, or chatter.

1.3.4 Sintering

Once formed and dried, a ceramic part is considered “green” until it is fired. Firing is the process of applying heat, and sometimes pressure, to a green part to generate the desired microstructure and bulk properties. Firing includes thermolysis of organic materials (such as pore formers, binders, etc.), followed by sintering. Development of the thermolysis step of firing for this work is discussed in Section 3.7. Sintering is the key step of the firing process because it is during sintering which the final microstructure of the part will be developed. In general, a fired part will be denser, less porous, and stronger than a green part.

Modes of sintering include solid state sintering, liquid phase sintering, reactive liquid sintering, and vapor phase sintering. We will consider only solid state sintering as it is relevant to this work.

Solid state sintering proceeds in three stages. In the initial stage, surface diffusion causes the ceramic particles to become more spherical and necks to form between particles. In some materials, evaporation and condensation of ceramic contributes to these phenomena. A small decrease in porosity is seen in this stage. In the intermediate stage, these mechanisms continue. In addition, grain boundary diffusion and diffusion through the atomic lattice cause the necks between particles to thicken and porosity to significantly decrease and to partially or fully close. Since mass is conserved, the part shrinks in this stage. In the final stage of sintering, diffusion continues to reduce

or eliminate closed porosity, and grain growth occurs in the ceramic crystal. The mechanisms by which mass transport during sintering proceeds are summarized in Table 1.3.

Table 1.3: Summary of mass transport mechanisms relevant to solid state sintering. Adapted from Reed, 1995.

Mechanism	Densification
Surface diffusion	No
Evaporation-condensation	No
Grain boundary diffusion	Yes
Lattice diffusion	Yes

Densification and volume shrinkage occurring during sintering can cause stresses to develop in the part and if the stresses are too great, cracking will occur (Largiller, 2012). Sintering layered composites further complicates the situation because shrinkage mismatch between layers can also be a source of cracking (Simchi, 2006)(Johnson et al., 2003).

Matching sintering shrinkage was crucial to this work and was a major factor in choosing to co-fire or sequentially-fire each pair of layers. If a particular layer had a sintering shrinkage close to zero, it could be beneficial to sinter serially with respect to the previous layer. But if a particular layer's shrinkage during sintering is close to that of the layer beneath it, these layers should be co-fired. In this way stress between layers which may cause cracking or delamination is minimized. The development of the firing process is described in Section 4.5.

2 Related works

William Jaques was the first to propose generating electricity from coal without the losses associated with combustion (Jacques, 1896). His apparatus consisted of a piece of coal suspended by platinum wire in a bath of molten potash. Air was bubbled through the potash to react with the carbon in the coal, producing CO₂ and electricity. His work is theoretically fundamental to the present work, but provides little insight into the topic of modern cell fabrication.

In the late half of the 1900s, the Siemens/Westinghouse Corporation spent significant resources developing a cathode-supported tubular SOFC for commercial power generation. That body of knowledge has provided a starting point for much of the field's advancement during the last 20 years, which is discussed here.

Relevant works are examined on the basis of material choice, cell design, and fabrication techniques. A summary of these works is given in Table 2.1.

Table 2.1: Summary of relevant design choices of related works.

Author and year	Cell design	Material choice	Fabrication techniques
Siemens/Westinghouse, as reported by Huang and Singhal (2013)	Tubular cathode-supported SOFC	Anode: Ni/YSZ or Ni/SSZ Electrolyte: YSZ or SSZ Cathode: Ca- and Ce-doped LMO	Cathode extruded, bisque lay-fired, then hang-fired. Electrolyte and anode applied by APS.
Bai et al. (2009-2011)	Conical anode-supported DCFC	Anode: NiO/YSZ Electrolyte: YSZ Cathode: LSM	Anode and electrolyte dip-coated onto conical form. Cathode painted on by brush.
Zhao et al. (2009)	Tubular cathode-supported DCFC	Anode: NiO/SSZ Electrolyte: SSZ Cathode: LSM	Cathode, electrolyte, then anode dip-coated onto glass form, then removed and co-fired.
Pati (2010)	Tubular electrolyte-supported DCFC	Anode: liquid alloy Electrolyte: YSZ Cathode: NiO/YSZ	YSZ electrolyte tube purchased, dip coated with cathode slurry.
Giddey et al. (2014)	Tubular electrolyte-supported DCFC	Anode: LCSF Electrolyte: YSZ Cathode: LCSF	YSZ electrolyte tube prepared by isostatic pressing. Cathode and anode ink painted on by brush.
ur Rehman et al. (2017)	Tubular cathode-supported DCFC	Anode: NiO/YSZ Electrolyte: YSZ Cathode: LSM/YSZ/GDC/AC	Cathode extruded, electrolyte and anode applied by dip coating.
Ido and Kawase (2020)	Tubular molten carbonate DCFC	Anode: Ni-AlCr Electrolyte: α -Lithium alumina/AC Cathode: Ni-MgO	Cathode slurry brushed onto metal pipe, then sintered. Electrolyte matrix and anode brushed on, then sintered. La/Ni carbonate powders applied and impregnated into anode and electrolyte matrix.
Kouchachvili et al. (2021)	Planar molten carbonate DCFC	Anode: Ni foam Electrolyte: (Li/Na/K)carbonates Cathode: NiO foam	Metal foam plates mounted to electrolyte matrix. Molten electrolyte circulated through.

Cell designs in Table 2.1 can be loosely organized as either planar or tubular, and having either a solid or a molten electrolyte. Planar designs suffer from difficulty sealing the oxidant gas away from the exhaust (Giddey, 2012). Tubular designs present challenges primarily in fabrication, which is the focus of the present work. Kouchachvili et al. claim that molten carbonate electrolytes are

favorable to solid oxide because they provide more opportunity for formation of the triple phase boundary required for the working reaction. They fail to consider a liquid anode design, which provides the same benefit.

The material choice for the cathode and electrolyte of the present work is informed primarily by the work of Siemens/Westinghouse. Many of the works in Table 2.1 use similar materials because they too are informed by the decades of progress by Siemens/Westinghouse. Pati's 2010 work is notable because it is one of only a few attempts to use a liquid metal alloy for the anode. Colet Lagrille's 2013 work discusses others. Ni-based materials are also popular for use in the cathode layer, but as discussed in Section 4.2, La-based materials are preferable because they match the thermal expansion coefficient of YSZ more closely.

Fabrication techniques vary quite widely between researchers. Siemens/Westinghouse, Pati, and Rehman use extruded ceramic tubes. The present work aims add simplicity and scalability to the fabrication process compared to these works. Bai et al. and Zhao et al. fabricate their support by dip coating onto a form. This technique lacks scalability because a new form must be manufactured to change the size of the cell. In addition, the process is long because it involves multiple dipping and drying steps for each layer. Siemens/Westinghouse use atmospheric plasma spray (APS) to apply their cathode and anode layers. This process is an improvement over their initial efforts with electrochemical vapor deposition (EVD) in terms of simplicity and expense, but still cannot compete with slurry coating in this regard. Bai et al. and Giddey et al. use brush painting to apply one or more layers to their supports. This technique can be appropriate for initial research, but is absolutely not scalable. In addition, moving from brush painting to an industrially feasible process such as dip coating may require a complete redesign—consider coating the inside of an open-ended tube. The fabrication process of Ido and Kawase is needlessly complicated by having to shave and punch a metal support and impregnate carbonates into the structure after it is fired. The method of slurry application is not given. Many of the examined works utilize dip coating in some part of the fabrication process. This is no surprise, as its versatility, simplicity, inexpensiveness, and in some embodiments, scalability, make it attractive as both a lab-scale and industrial-scale technique.

Siemens/Westinhouse use multiple firing steps which each require specialized equipment, which is not desirable. The most attractive sintering process is that of Zhao et al., who co-fire their cell. Yoon et al. use this technique in their 2009 work as well; their work is not examined here because it is neither of tubular nor SOFC design, but is discussed in Section 4.5.

3 Methodology

3.1 Slurry preparation

To prepare the slurries, components were weighed and mixed overnight by ball milling with 4mm diameter alumina media.

3.2 Zeta potential characterization

Two types of zeta potential testing were performed in this work: pH sweeps and surfactant concentration sweeps. For both methods, a 2% wt dispersion of analyte powder in DI water was prepared, and then sonicated for 5 minutes and about 12 kJ of energy with a Misonix S-4000 Sonicator. The sonicated dispersion was transferred to a Colloidal Dynamics ZetaProbe. For pH sweeps, the basic titrant was a 0.5M KOH solution and the acidic titrant was a 0.5M HNO₃ solution. For surfactant concentration sweeps, the titrant was a 10 wt% solution of Dolapix CE-64 in DI water.

3.3 Rheology characterization

A Discovery HR-1 rotational rheometer from TA Instruments was used for the rheology studies in this work. It was equipped with a 2° cone and plate geometry. The method consisted of a constant shear rate of 1 s⁻¹. This low shear rate was selected to represent the shear on the drying slurry due to gravity and is common for ceramic slip characterization (Reed, 1995). The test lasted either 1 or 2 minutes.

3.4 Slip casting

Pottery plaster #1 was purchased from the United States Gypsum Company. Plaster and DI water were mixed in a mass ratio of 10 to 7. For initial experiments, the plaster was poured into a plastic container case mold and a 1" diameter aluminum rod was suspended in the plaster as it dried, according to Figure 3.1. Once the plaster dried, the rod was removed, leaving a negative space into which the slip was poured for casting. The apparatus for this is shown in Figure 3.1.



Figure 3.1: Initial setup for creating slip casting molds. The plaster was poured around the suspended rod, and once dry, the rod was removed.

This process was later refined. The plaster was prepared in the same way and then poured into smaller case molds and allowed to dry. Then, a shallow tube was drilled into the plaster with a ball-end router tool, which is shown in Figure 3.2 along with the plaster mold it is used to create. This method has the advantage of creating a cavity with a hemispherical bottom. This minimizes stress concentrations due to shrinking while drying and sintering, compared to the previous flat-bottomed cylindrical molds. A shallow bevel was cut around the edge of the hole with a utility knife so that the cast part would have a flange from which it could be hung during the dip coating process. During casting, the cavity was constantly refilled with slip as the water was absorbed into the mold. The casted part was left to dry in the mold overnight or until it had dried enough to pull away from the mold and be easily removed.

Casting time was on the order of minutes but was varied as a parameter of study. A successful cast did not crack, released well from the mold, and had sufficient green strength for further processing.



Figure 3.2: Hemispherical-bottomed mold, and the ball-end router tool used to create it.

Cast slip was not recycled because it was found that recycled slip cracked in the mold when recast. This is likely due to the faster drying rate of cast slip due to its higher solids content (Reed, 1995). The increased solids content is the result of the water being drawn out by the mold during casting, before the excess slip is recycled back into the container for re-use.

3.5 Porosity characterization by Archimedes method

Density of fired parts was measured by the Archimedes method. In this method, the dry weight w_{dry} of a fired part is measured, and then the part is dipped in a tank of molten paraffin wax until it is well coated. The waxed weight w_{waxed} is recorded. Then the coated sample is submerged in water and the submerged weight w_{wet} is recorded as well. The density of the part ρ is calculated as

$$\rho = \frac{w_{dry}}{w_{waxed} - w_{wet} - \left(\frac{w_{waxed} - w_{dry}}{\rho_{wax}} \right)} \quad (3.1)$$

The porosity of the part, p , may then be calculated as

$$p = 1 - \frac{\rho}{\rho_{theoretical}} \quad (3.2).$$

3.6 Dip coating of cathode and electrolyte

The cast LCM support, once removed from its mold, was first thoroughly dried in an Across International CF-1700 muffle furnace at 50°C for 30 minutes. This drying step increased the green strength of the cast.

While the cast was drying, the cathode and electrolyte coating baths were prepared. Initially, the coating bath was a 40mL beaker. Later, to accommodate longer parts, a 250mL graduated cylinder was used. The appropriate coating slurry was stirred and then transferred to the coating bath slowly to prevent air entrainment.

The dried support was held with tweezers, dipped into the coating bath, withdrawn, and then hung by its flange on a wire holder. The dip coating process is shown in Figure 3.3 and coated parts hanging in their holders are shown in Figure 3.4.



Figure 3.3: A dry support which has just been dip coated with cathode slurry.



Figure 3.4: Dip-coated samples resting in their holders. Left: a dry cathode coating. Right: a dry electrolyte coating.

The wire holders were made by bending stainless steel wire into the appropriate shape. The part was left hanging on the holder until the most recent coating was dry to the touch.

3.7 Firing

An Across International CF-1700 muffle furnace equipped with a B type thermocouple was used for firing of all samples. Samples were lay-fired in the tray pictured in Figure 3.5 , which is designed to maintain the roundness of the tube as it shrinks during sintering and produce a tube of uniform sintered diameter.



Figure 3.5: Firing trays used to lay-fire samples.

Two firing programs were used, depicted in Figure 3.6 and Figure 3.7.

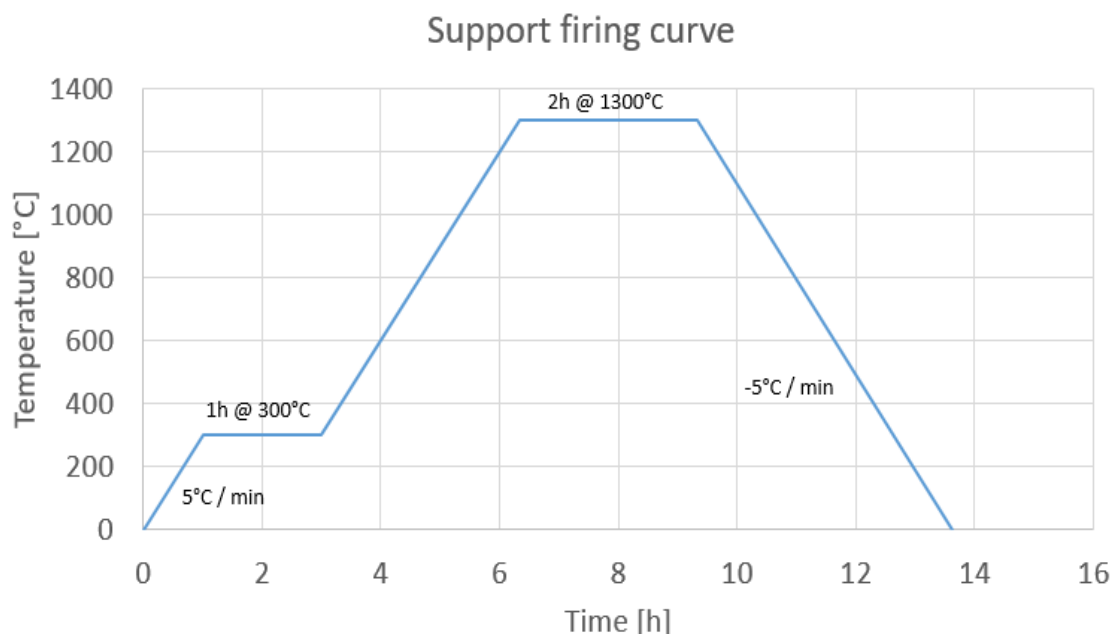


Figure 3.6: Firing curve #1. This curve is used when the sample being fired is an LCM support.

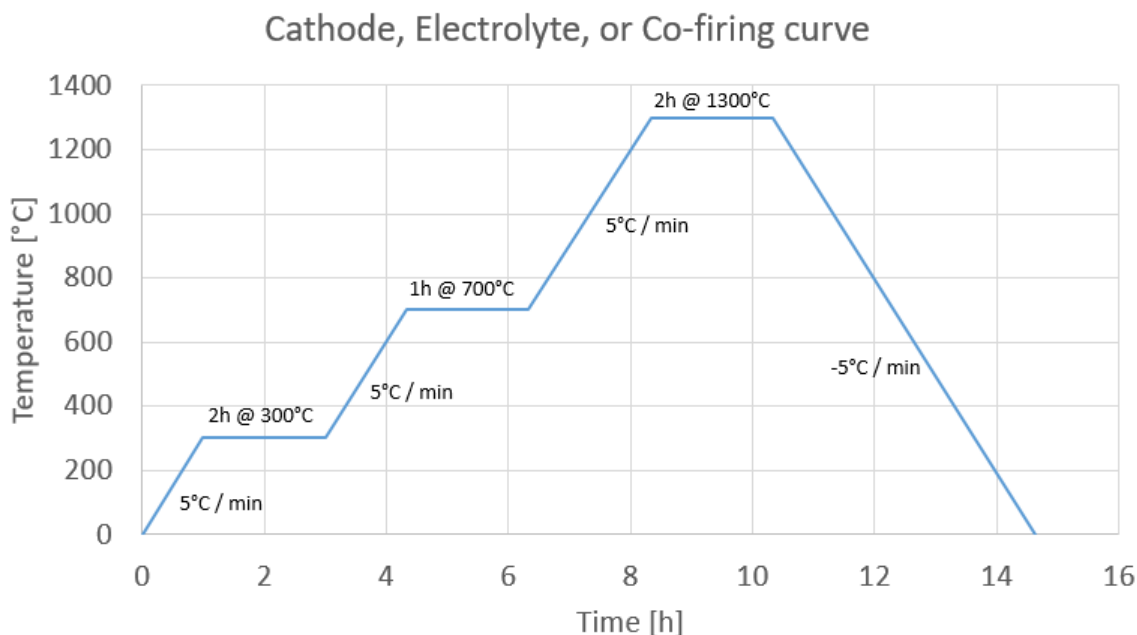


Figure 3.7: Firing curve #2. This curve is used for sintering samples which include a cathode layer. (Yoon, 2008).

Curve #1, depicted in Figure 3.6, is used for sintering support samples only. The 2 hour hold at 300°C is designed to burn out the cellulose pore former and the dispersant. Curve #2 adds a 1 hour hold at 700°C to burn out the carbon black pore former in the cathode layer. Curve #2 mimics the

firing process used by Kyung Joong Yoon for co-firing planar SOFC composites from similar materials.

Both curves share a common 2 hour hold at 1300°C to sinter the part, per the 2008 work of Yoon, et al. This temperature is selected to produce a fully densified electrolyte while preventing the support from over-sintering. In addition, a small amount of nanoalumina is used in the electrolyte layer as a sintering aid (Yoon, 2008). Over-sintering of the support is not desirable because too much densification would result in closing the open porosity which is required to deliver oxygen to the cathode, where it is ionized.

3.8 SEM imaging

Before imaging, the part is sectioned with an abrasive saw to produce a flat surface. Then, a mixture of 3 parts Buehler EpoxiCure 2 Epoxy Resin to 1 part Buehler EpoxiCure 2 Hardener is prepared. The sectioned part is mounted in a mold and the mold is filled with the epoxy mixture. The filled mold is held overnight under vacuum in a vacuum desiccator. The cured pucks are removed from the mold and polished with a Buehler AutoMet 250 polishing machine with an appropriate method and abrasives.

The polished samples are examined with a Hitachi TM3030 scanning electron microscope (SEM) operating at 15kV acceleration voltage in backscatter detection mode.

3.9 Cell testing

3.9.1 Alloy preparation

Alloy 1, described in Table 1.1, was used as the anode for this work. It was prepared by adding the component metals to a crucible and melting until combined. A 2000g batch of components was prepared, mixed, and divided into four 500g samples. Each sample was placed in a fireclay crucible surrounded by the heating elements of an Ambrell EasyHeat 8310 LI heater. Another fireclay crucible was placed, inverted, atop the one containing the sample. The top crucible had a port for the argon lance which delivered argon gas at a flow rate of about 4L/min for the duration of the process. It also contained a viewport so that temperature could be measured by pyrometer. The setup is described by Figure 3.8. The alloy was heated to about 1400°C for about 5 minutes. Once melted and cooled, the 500g samples were cut into approximately cubic chunks, about 1cm on a side, with an abrasive saw.



Figure 3.8: Setup used to melt the anode alloy.

3.9.2 Apparatus description and preparation

The testing apparatus was a Mellen induction furnace with a customized testing insert comprised principally of a platform suspended by threaded rods from a flange. The flange is removable and rests upon a steel pipe set vertically into the furnace. Through the flange are the necessary couplings for thermocouples, inert gas feed, electrolyte tube, and fuel/current collector rod. The apparatus is depicted in Figure 3.9 and described thoroughly in Faria's 2021 work.

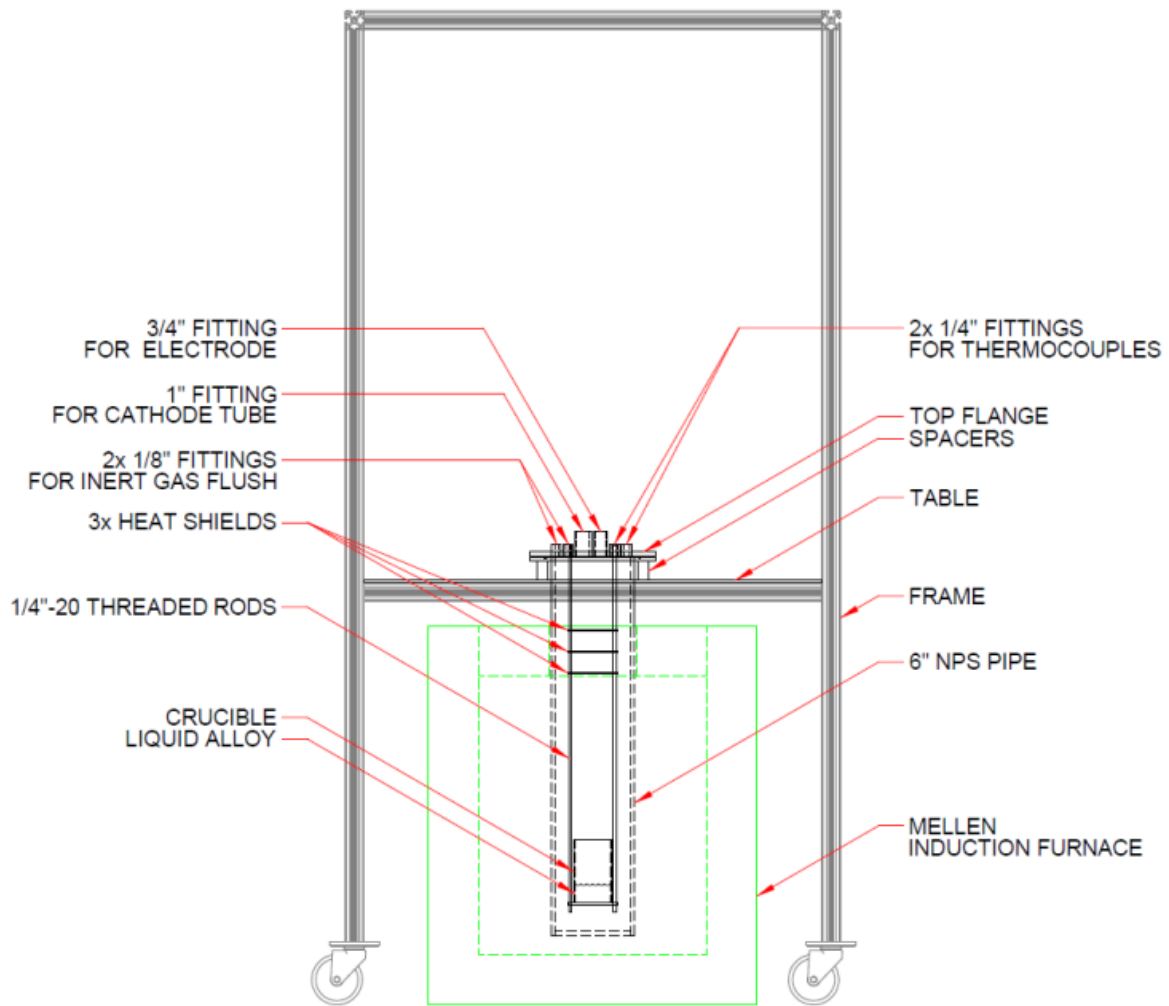


Figure 3.9: High-temperature electrochemistry apparatus, from Faria (2021).

Ceramabond 503 ceramic cement from Aremco was used to affix the cathode-electrolyte structure described by Figure 4.30 to the end of a 1" diameter open-ended mullite tube. The mullite tube is necessary to provide mechanical support to the cathode-electrolyte structure as it hangs from the flange in the furnace. This assembled structure was inserted through the flange and suspended about 1cm above the bottom of an alumina crucible which rested on the bottom plate of the testing insert. Through the other hole in the flange a graphite rod was inserted and hung similarly in the crucible. The graphite rod acted as both the fuel source and the anodic electrical contact. The chunks of anode alloy were piled around the cathode-electrolyte structure in the crucible. A length of Kanthal wire was inserted into the mullite tube until it made contact with the inside of the cathode-electrolyte structure. This served as the cathodic electrical contact. The testing insert was lowered into the furnace and sealed. The prepared testing insert is depicted in Figure 3.10.



Figure 3.10: Testing insert for which was used to suspend the anode-containing crucible, cathode-electrolyte structure, and graphite fuel rod in the furnace.

The furnace which houses the testing insert is shown in Figure 3.11.



Figure 3.11: The Mellen induction furnace used to test the cell. The testing insert is inserted into the hole. The testing insert's flange is supported by the flange of the furnace tube.

Argon gas was injected into the furnace through the flange at a flow rate sufficient to maintain less than 0.5% oxygen in the testing chamber. Air was injected into the mullite tube through a nozzle to provide the cathode with oxygen atoms for ionization.

3.9.3 Apparatus operation and measurement

The furnace was heated to 950°C at a rate of 10°C/min, and then to 1000°C at a rate of 2°C/min. The open circuit voltage (OCV) was measured by handheld multimeter at the kanthal wire extending from the cathode and at the graphite rod extending from the anode.

4 Development

4.1 Fabrication process overview

A simple description of the fabrication process for the cathode-electrolyte structure is: the support/current collector is slip casted, and then the cathode and electrolyte are sequentially dip-

coated upon it. Understanding this general idea gives context to the development work which follows. The process in slightly more detail is given in Figure 4.1 as a reference.



Figure 4.1: The generalized process followed to fabricate cathode-electrolyte structure prototypes.

It is important to note that this figure is presented as a reference for context, not as an accepted optimal process. While each step was developed with the preceding and following steps in mind, minor steps were added and removed as necessary for development. Notably, the firing and drying steps were moved and modified as development progressed. However, it was obvious from the outset that each layer would eventually need to be dried and fired for the final structure to take shape. Figure 4.1 reflects that fact and emphasizes that no step in the fabrication process could be developed in a vacuum; each influences the rest.

4.2 Active material choice

The choice of active materials for the current collector, cathode, and electrolyte build on the work done by Yoon, et al. in 2008. LCM is used for the current collector to maximize electrical conductivity and minimize thermal expansion mismatch between the layers of the structure. A blend of LCM and YSZ is used in the cathode to create a shallow thermal expansion coefficient gradient between the current collector and electrolyte, again minimizing thermal expansion mismatch. YSZ is used in the electrolyte because it is widely used in solid-oxide fuel cell (SOFC) technology for its high oxygen ion conductivity. In addition to matching thermal expansion coefficients to prevent delamination during cell heat-up and operation, these materials have similar sintering shrinkages, allowing them to be co-fired (Yoon et al., 2007). There is also minimal chemical interaction between layers when LCM and YSZ are used in this manner (Yoon et al., 2007).

For this work, LCM powder with 5% A-site deficiency, 20% Ca dopant, and surface area of 5-8 m²/g was purchased from Nexceris as a custom order. A-site deficient LCM is selected because such deficiency lowers the sintering temperature, increasing co-firing compatibility with YSZ. (Jiang, 2008). YSZ powder containing 8 mol % yttria and having a surface area of 1-3 m²/g (part number 312008) was also obtained from Nexceris. YSZ with 8 mol % yttria is selected because it is considered fully doped, maximizing the oxygen ion vacancies and therefore the ion transport in the electrolyte.

Water was chosen as the solvent for all three slurries, because when possible, the more environmentally friendly solvent is always the better option.

4.3 Formulation

4.3.1 Powder characterization by zeta potential

The LCM was first characterized by pH sweep and the results are given in Figure 4.2.

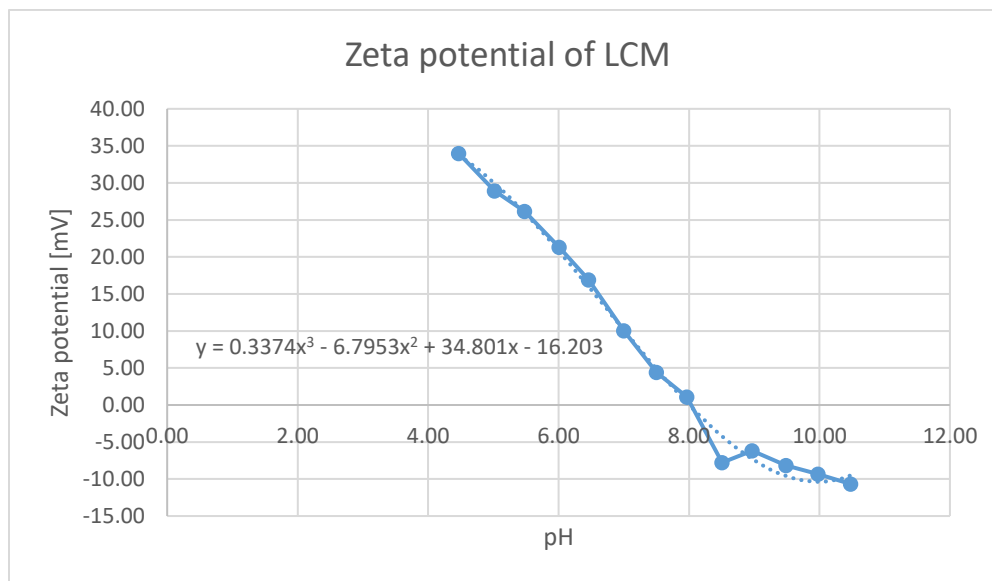


Figure 4.2: Zeta potential of LCM over a range of pH.

As can be seen, LCM in water does not reach a ZP of ± 40 mV at any reasonable pH. This indicates that a surfactant would be required to ensure stable dispersion of the LCM in water. Since LCM in water does not have a strong positive nor negative charge, either a cationic or anionic surfactant may be employed. The anionic dispersant Dolapix CE-64 from Zschimmer & Schwarz was selected.

Next, a new sample was characterized by surfactant concentration sweep. The data is plotted as a function of mass ratio of active surfactant material to LCM so that it may be used to guide formulation. These results are shown in Figure 4.3, which confirms that Dolapix CE-64 is a strong anionic dispersant in this system. However, though it has a strong influence on ZP, pH was measured but not controlled in this experiment. To account for this, the ZP vs pH data in Figure 4.2 is used to adjust the data in Figure 4.3 for pH. First, a polynomial line of best fit is fit to the ZP vs pH data. This model is used to calculate, for each point of the ZP vs surfactant mass ratio data, what the ZP would be at the relevant pH without any surfactant. Finally, the pH-corrected ZP of the LCM at various surfactant mass ratios is calculated as

$$\zeta_{corrected} = \zeta - \zeta_{equivalent\ pH} \quad (4.1).$$

The corrected ZP is shown in Figure 4.4. From this data, it is evident that a surfactant-to-powder mass ratio of 6% will provide good electrostatic stabilization and prevent agglomeration, so this was taken as the target for formulation.

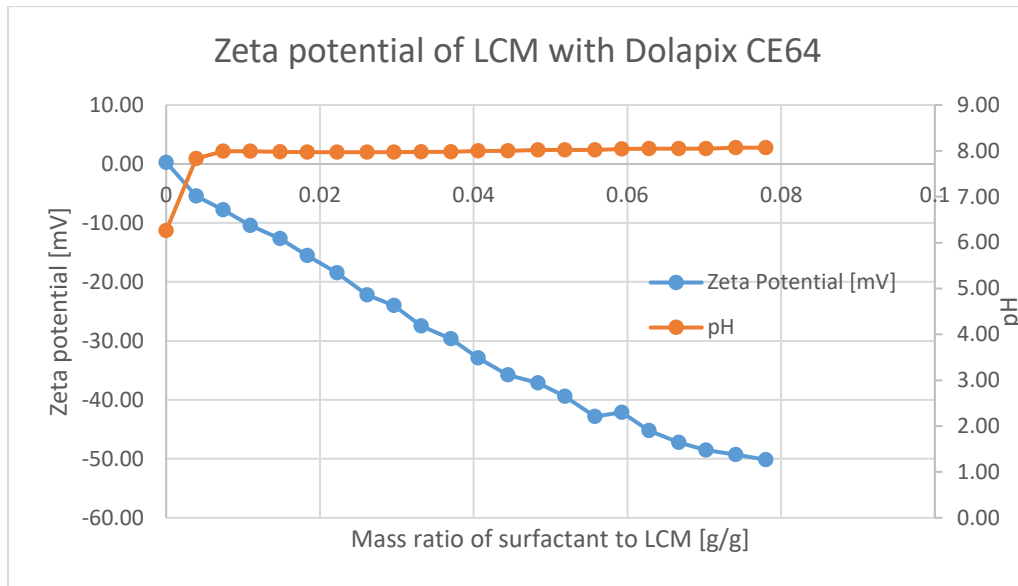


Figure 4.3: Zeta potential of LCM in DI water as concentration of Dolapix CE-64 is increased.

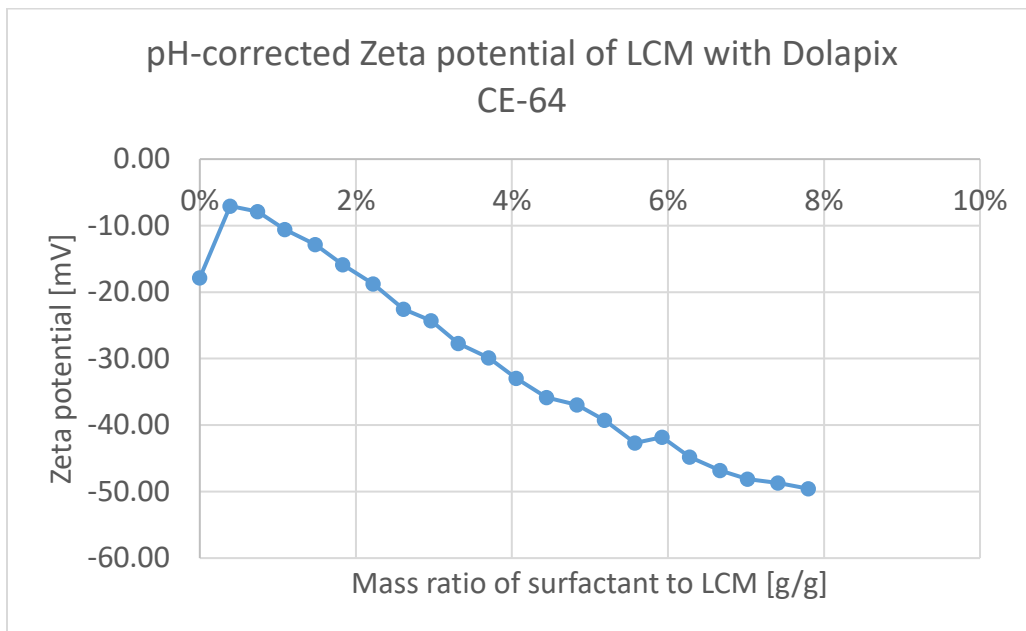


Figure 4.4: pH-corrected ZP of LCM with Dolapix CE-64 dispersant. A ZP of ± 40 mV is considered to give good dispersion stability (Kumar and Dixit, 2017).

The same process was followed for calculating the optimal dosage of surfactant in the YSZ electrolyte slurry. The zeta potential of YSZ as a function of pH, as a function of surfactant concentration, and as a pH corrected value are shown in Figure 4.5, Figure 4.6, and Figure 4.7, respectively.

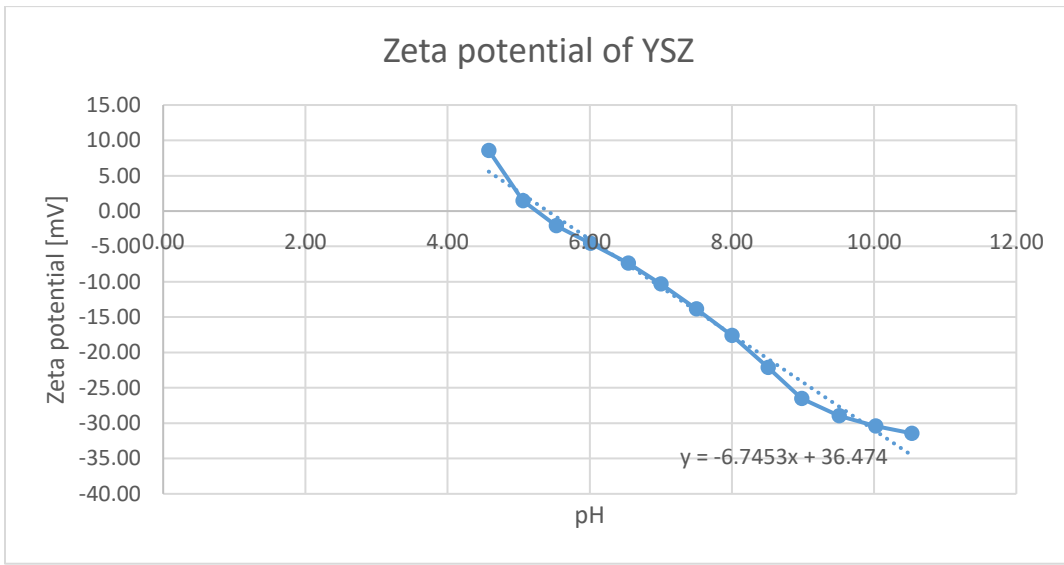


Figure 4.5: Zeta potential of YSZ in DI water as a function of pH.

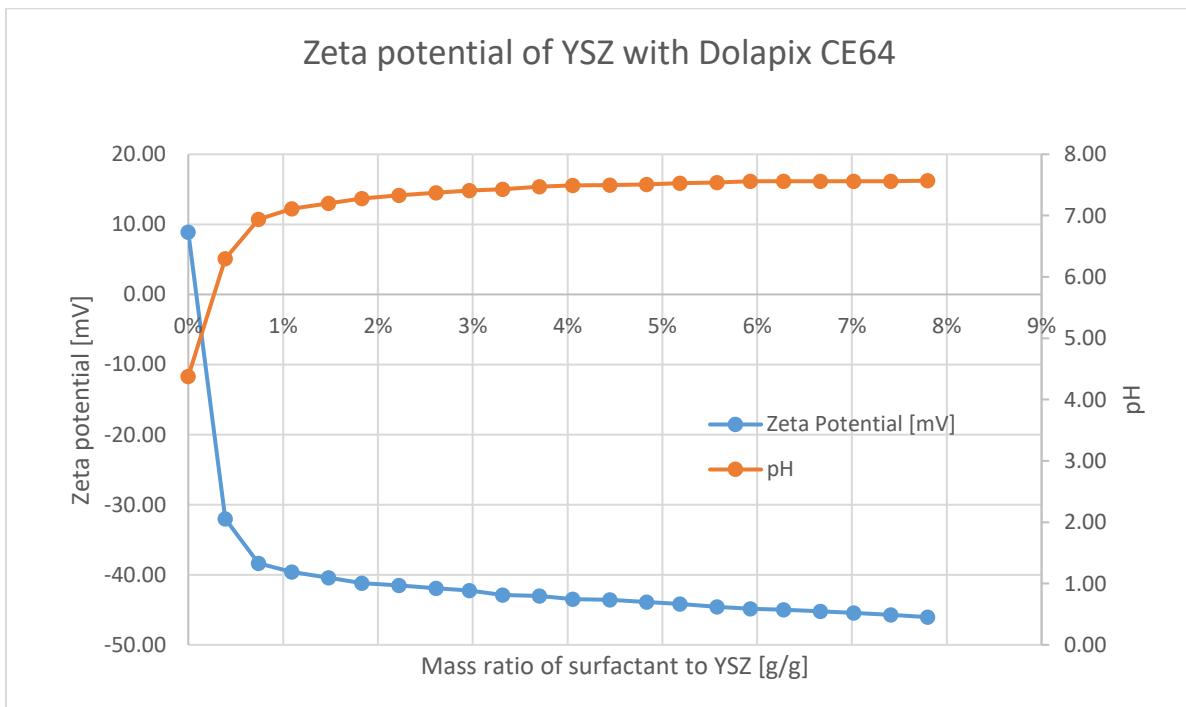


Figure 4.6: Zeta potential and pH of YSZ in DI water as Dolapix CE-64 concentration is increased.

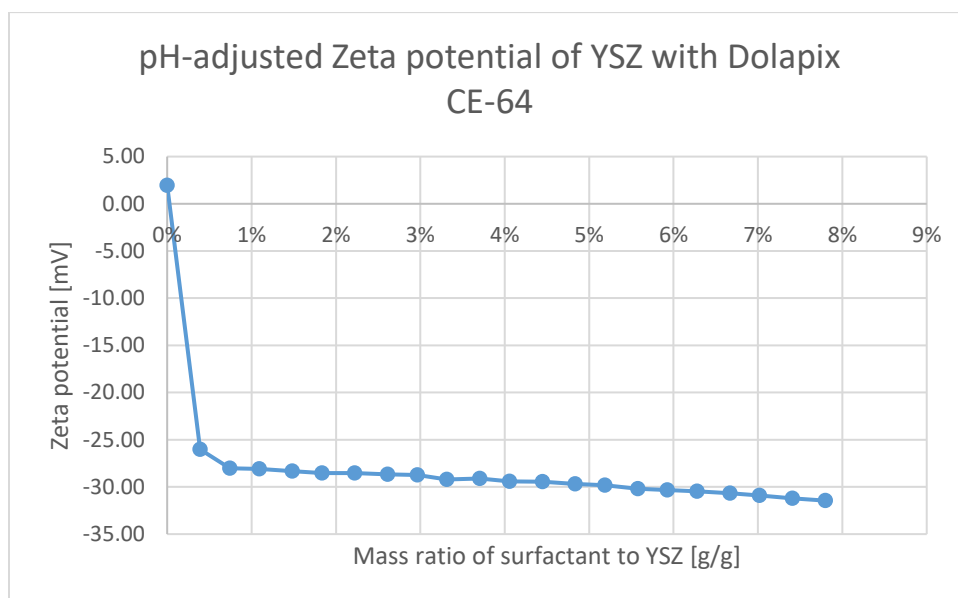


Figure 4.7: pH-corrected ZP of YSZ with Dolapix CE-64 dispersant. A ZP of ± 40 mV is considered to give good dispersion stability (Kumar and Dixit, 2017).

The curve in Figure 4.7 shows that a ZP of -40mV is not achievable with a reasonable amount of Dolapix CE-64 in this system. In addition, there is no significant benefit to increasing the surfactant-to-powder ratio beyond 1%, so this is taken as the target for formulation.

4.3.2 LCM support/current collector formulation

The general formulation of the LCM support is given in Table 4.1.

Table 4.1: General formulation of the LCM support.

Material	Purpose	Amount
LaCaMnO ₃ (LCM)	Active material	20-40 wt % on total wet weight
Dolapix CE-64	Dispersant	6 wt % on weight of LCM
20 μ m cellulose	Pore former	50 vol % on dry volume
PVA	Binder	0-2 wt % on total wet weight
DI Water	Solvent	50-70 wt % on total wet weight

Section 4.2 explains the choice of active material. 20 μ m cellulose was chosen as the pore former because as explained in Section 1.2.2, it is important to maximize gas flow through the support for good cell performance. The cellulose was obtained from Sigma Aldrich (part number 310697). PVA was used as the binder as it is commonly used in slip casting to give good green strength at low concentrations (Reed, 1995).

The first experiment with the support had the goal of optimizing the binder content. Too little binder can give poor green part strength, but too much binder can increase viscosity to the point of processability issues (Reed, 1995), so the level must be carefully controlled. Samples with 0, 0.25, and 0.5 wt % binder on weight of active powder were formulated and cast. These samples are shown in Figure 4.8. It should be noted that these samples were made with Lanthanum Strontium Manganite (LSM), instead of LCM, due to temporary unavailability of LCM. The LSM was also obtained from Nexceris (part number 121101) and has properties similar to LCM. It should also be noted that these samples did not contain pore former.



Figure 4.8: Casted supports with varying levels of PVA binder. Note that these samples were made with LSM rather than LCM and did not contain pore former.

All samples released well and had adequate green strength. However, the low binder sample had noticeably thinner walls at the top than the bottom. This is an indication that the viscosity of the slurry was too low and that the cast slumped during drying. For each sample, the thickness of the walls was measured at the top and the bottom of the part and the difference divided by the height of the part was reported as taper. Low taper is desirable because uniform wall thickness is expected to lead to uniform cell performance.

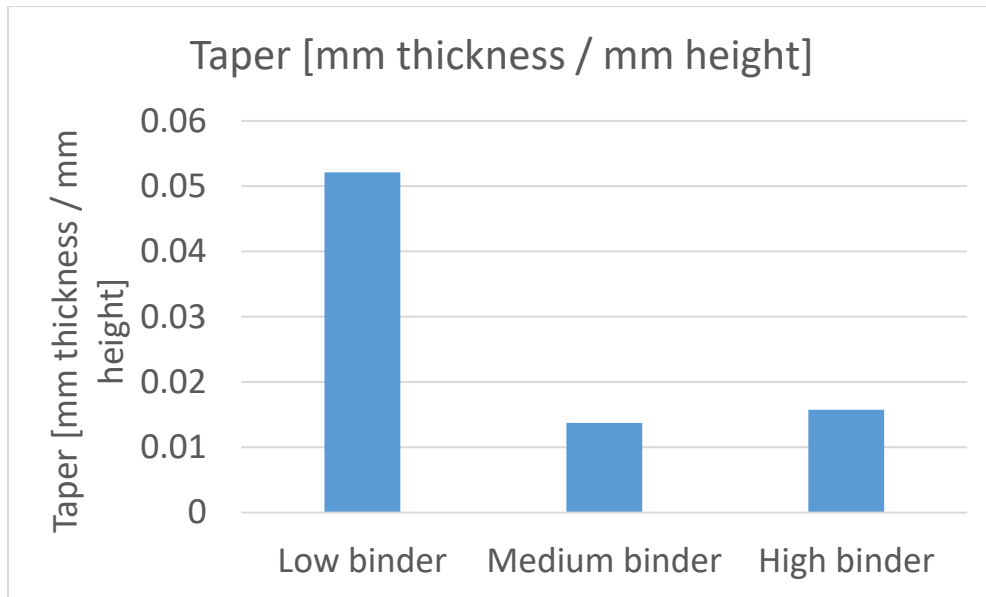


Figure 4.9: The taper of the walls in 3 support casts vs the binder content. The taper is calculated as the wall thickness at the top minus the wall thickness at the bottom, all divided by the height of the part. Note that these parts were made of LSM instead of LCM.

The rheology of each sample was measured according to the method described in Section 3.3 and the results are shown in Figure 4.10.

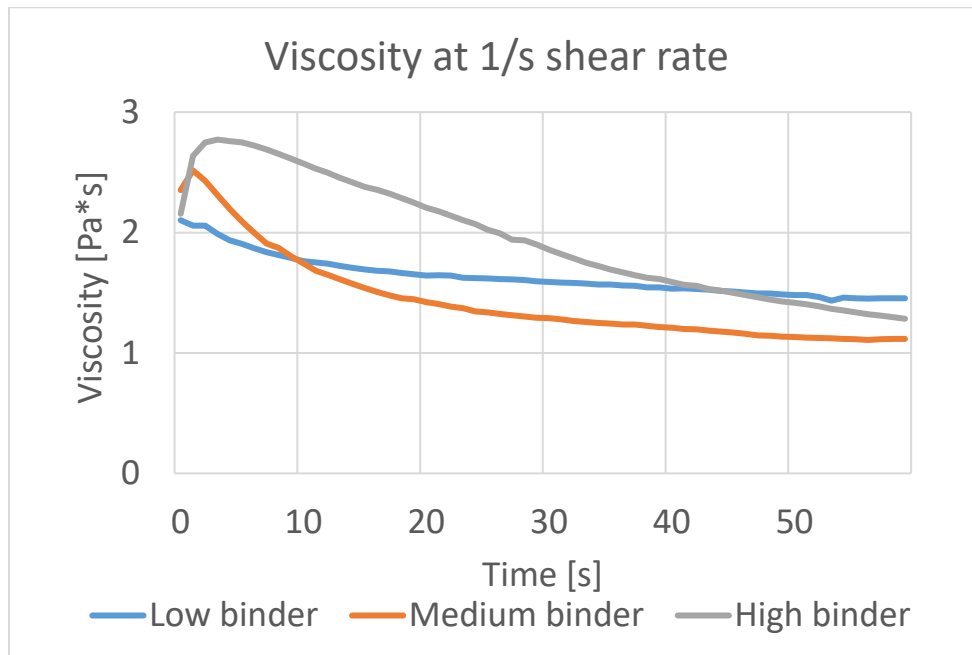


Figure 4.10: Rheology of LSM samples with various binder amounts. Tested with 2° cone and plate geometry.

Interestingly, the low binder sample displays higher viscosity than the medium binder sample over much of the time of the test. However, from the taper measurements, we know that the low binder sample slumps more than the medium binder sample during drying. The potential explanation for this is that since samples dry quite quickly in the mold, only the rheology at very short times is relevant. Indeed, the viscosity of the low binder sample is lower than that of the medium binder sample until the 10 second mark. The crossover in viscosity at 10 seconds is likely due to a thixotropic effect the study of which is outside of the scope of this work.

The conclusion of this experiment is that for samples with no pore former, 0.25 wt % binder on weight of active powder is enough to give adequate viscosity to avoid slumping in the mold. This same level of binder gives adequate green strength.

Next, the optimization of pore former content is pursued. A target of 50% porosity is chosen after the 2010 work of Yoon et al. who showed good performance with an LCM current collector of 50% porosity.

Samples formulated to 50% dry volume of cellulose were cast. They released well from the mold and had adequate green strength. They were fired according to Figure 3.6. At this point in the development process it was not clear whether the final composite would be co-fired or sequentially fired. These samples were sent through 1, 2, or 3 firing cycles to determine if multiple firing cycles would significantly alter the porosity. Figure 4.11 shows that multiple firing cycles do not dramatically alter the porosity of the LCM support, but that only about two-thirds of the formulated porosity is achieved after firing.

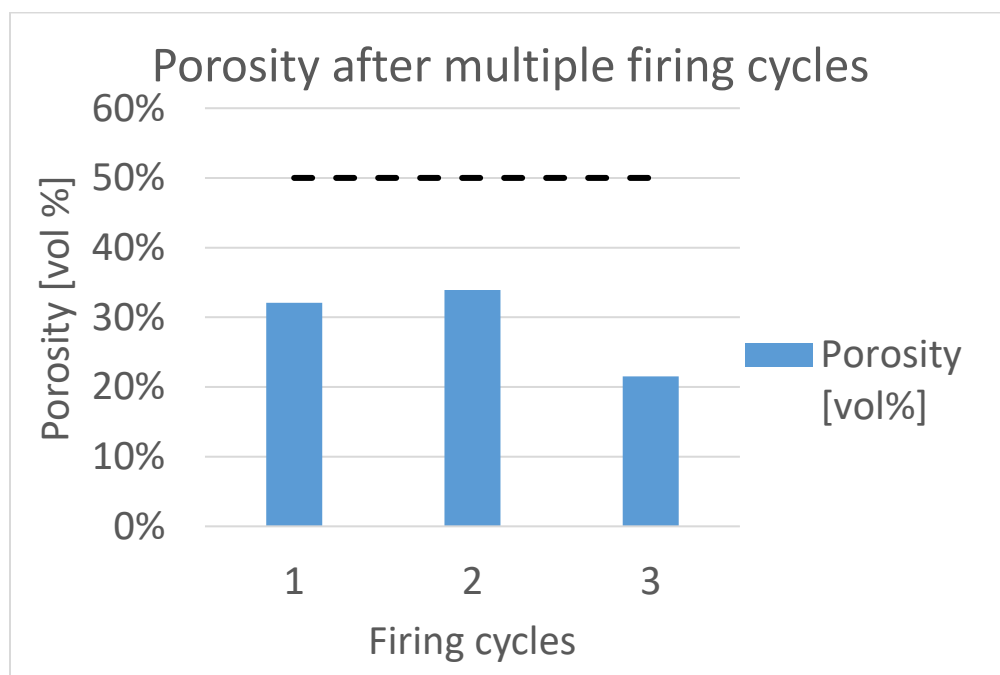


Figure 4.11: Porosity of LCM support after 1, 2, and 3 firing cycles of Curve #1.

The next set of samples were formulated to 77 dry volume % cellulose because it was expected that they would densify to the 50% target during firing. These samples were similarly sent through 1, 2, and 3 firing cycles. Porosity measurements after firing are shown in Figure 4.13. As expected, the samples densified to about two-thirds of the formulated porosity, reaching the target of 50%. The porosity did not change after multiple firing cycles. Unfortunately, the samples cracked in the mold during drying, an example of which is shown in Figure 4.12.



Figure 4.12: An LCM support sample which has cracked in the mold.

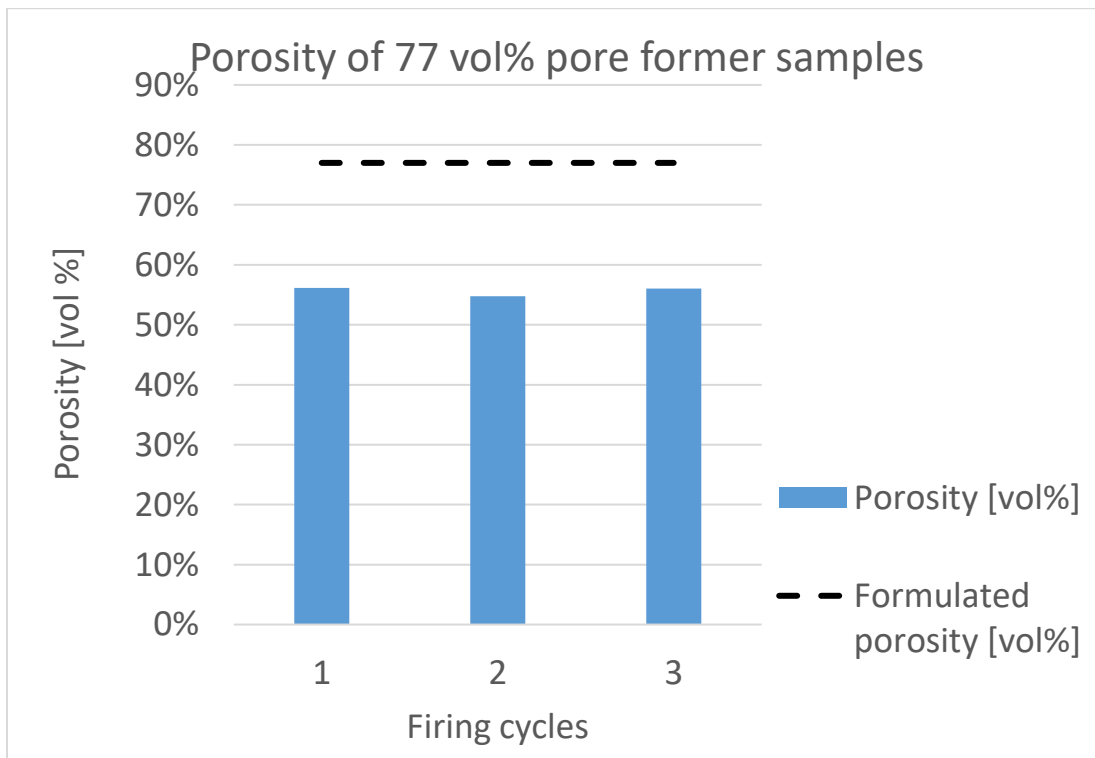


Figure 4.13: Porosity of LCM samples formulated to 77 dry volume % cellulose after various firing cycles of firing Curve #1.

Additionally, processing the slurry formulated to 77% porosity presented difficulty. Filtering out the mixing media was difficult due to the high viscosity, shown in Figure 4.14. For reference, the viscosity curve from the 0.5 wt % binder sample in Figure 4.10 is reproduced. The 77% porosity sample's viscosity is approximately an order of magnitude higher. This high viscosity also led to problems during casting. Although the samples in both Figure 4.8 and Figure 4.12 were casted for 5 minutes, the sample in Figure 4.12 has much thicker walls due to its viscosity. This is an indication that the viscosity is too high, because the cast thickness is optimally controlled by the casting time (Reed, 1995).

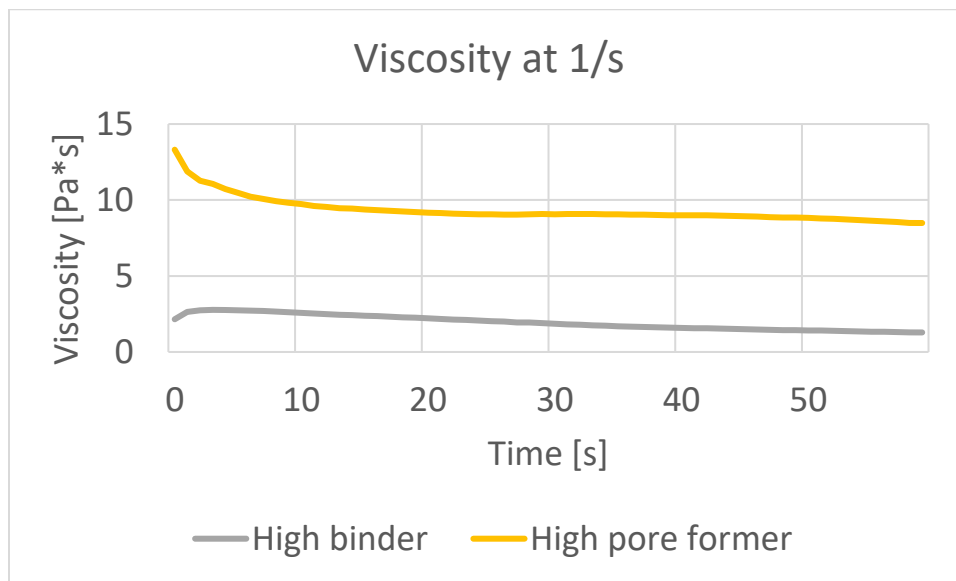


Figure 4.14: Viscosity of LCM slurry formulated to 77 dry volume % pore former and low binder content compared to a slurry formulated with a high binder content but no pore former.

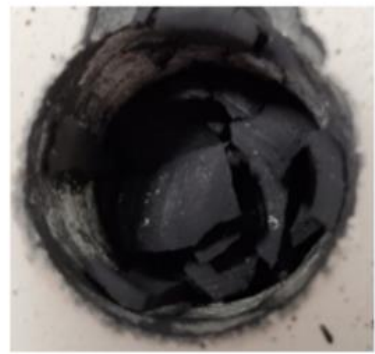
Nevertheless, in order to achieve the target porosity, 3 more samples were produced with higher binder to powder ratios. The hypothesis was that more binder in the dry cast would provide additional green strength, preventing cracking. Samples formulated to 3.9%, 4.9%, and 5.75% wt PVA on weight of LCM, all with 77 dry volume % cellulose pore former, are shown in Figure 4.15. Clearly, any additional green strength gained from the additional binder was not sufficient to prevent cracking.



**Low binder /
powder ratio**



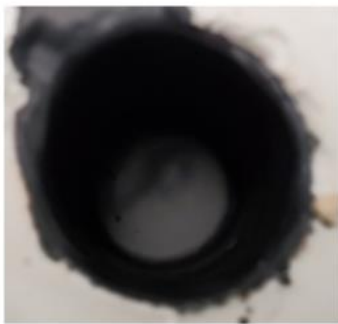
**Medium binder /
powder ratio**



**High binder /
powder ratio**

Figure 4.15: LCM casts with various binder to LCM ratios. All samples were formulated to 77 dry volume % cellulose pore former.

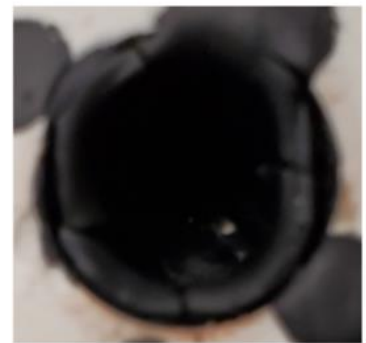
With options for fabricating supports with 77% formulated porosity exhausted, a ladder study to determine the maximum formulated porosity was conducted. Samples were formulated to 50%, 58%, and 67% porosity and then cast. Unfortunately, as depicted in Figure 4.16, the sample formulated to 50 dry volume % pore former was the only one which did not crack in the mold.



50% pore former



58% pore former



67% pore former

Figure 4.16: Cast supports which have been formulated to various porosities. The sample containing 50 dry volume % pore former was the only one which did not crack in the mold.

The broken pieces of each sample were fired and their density was determined by the Archimedes method. As shown in Figure 4.17, the trend of achieving about two thirds of the formulated porosity after firing continued.

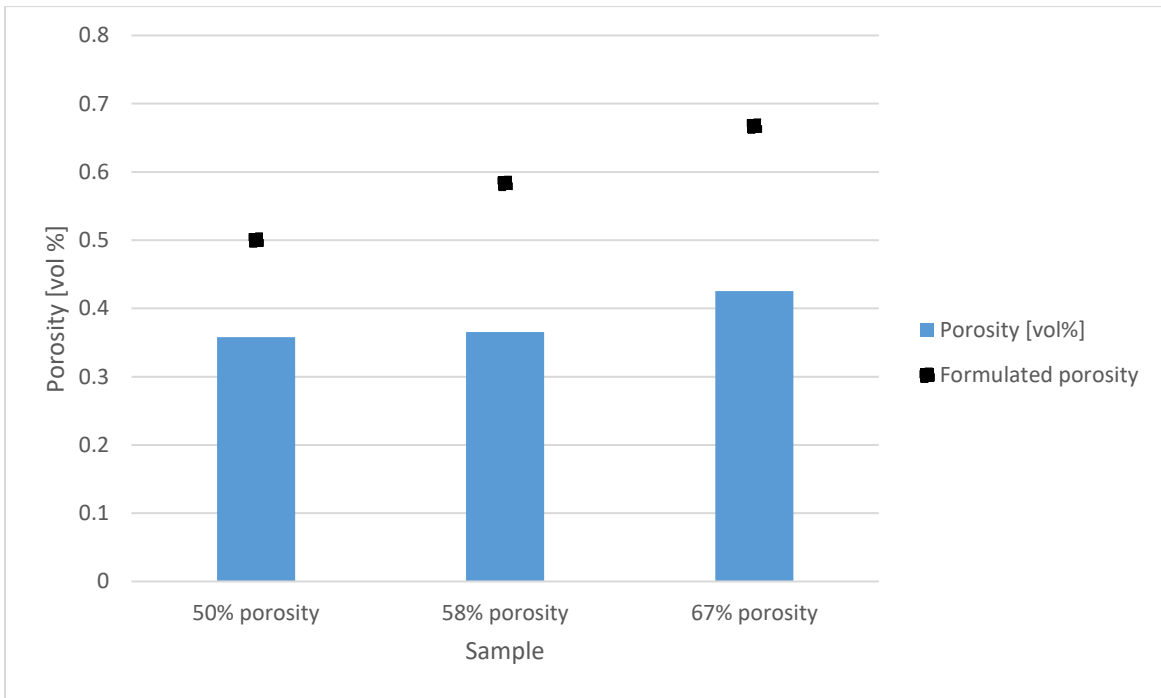


Figure 4.17: Formulated and fired porosity of samples made with various formulations.

As a result of this experiment, 50% formulated porosity was accepted as the maximum for this work. Possible strategies for increasing the porosity are discussed in Section 6.

The final formulation of the LCM support is given in Table 4.2. This formulation was used throughout the remainder of this work.

Table 4.2: The final formulation for the LCM support.

	wt %
LCM	40.06%
Dolapix CE-64	4.01%
Cellulose	3.69%
PVA	0.80%
DI Water	51.44%

4.3.3 LCM/YSZ cathode

The initial formulation for the cathode slurry is given in Table 4.3.

Table 4.3: The initial formulation for the cathode slurry.

	wt %
LCM	17.51%
YSZ	17.51%
Dolapix CE-64	2.89%
Carbon black	14.49%
PVA	0.93%
Water	46.68%

The weight ratio of LCM and YSZ is kept to 50-50 so that the thermal expansion and sintering shrinkage of the LCM support and the YSZ electrolyte remain compatible. The Dolapix dispersant is used at a concentration of 4 wt % on weight of active powder to account for the fact that the LCM requires 6% and the YSZ requires only 1%. The initial amount of PVA binder is 2 wt % on weight of water, which is the maximum recommended (Reed, 1995). The maximum is naïvely selected to give a high viscosity which will prevent settling in the slurry. The amount of carbon black is selected to give 40% porosity, as this level of porosity has been shown to give good performance in tubular SOFC cathodes (Zhao et al., 2009).

Two grades of carbon black from Cabot, Regal 250R and ELFTEx 320, were tested in the cathode slurry. Both grades have an average primary particle size of 5 μ m. The Regal 250R is powdered while the ELFTEx 320 is pelletized. The ELFTEx 320-containing slurry processed well. The slurry using Regal 250R was too viscous and did not mix well overnight in a ball mill. It was diluted and remixed per the formulation in Table 4.4.

Table 4.4: Formulation for the cathode slurry using Regal 250R carbon black.

	wt %
LCM	13.68%
YSZ	13.68%
Dolapix CE-64	2.26%
Carbon black	11.32%
PVA	0.73%
Water	58.35%

Small samples of both the remixed Regal 250R slurry and the ELFTEx 320 slurry were slip cast and fired, and their porosity was determined with the Archimedes method. The result is shown in Figure 4.18.

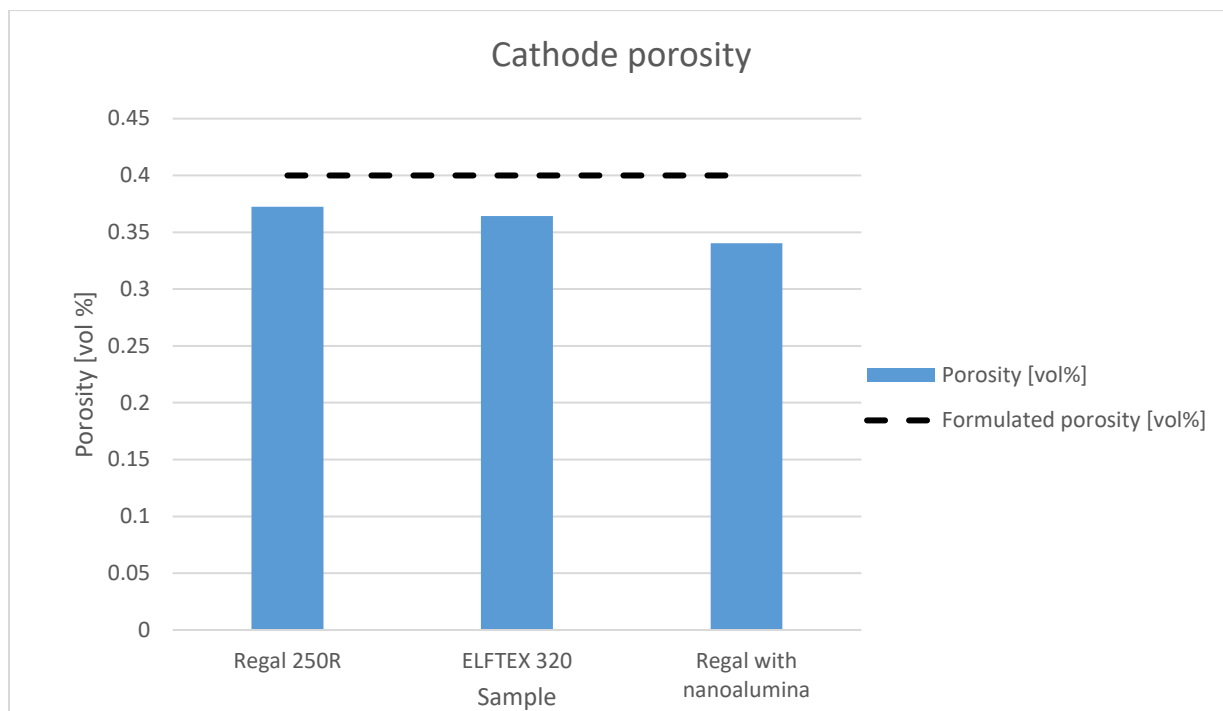


Figure 4.18: Fired and formulated porosity of cathode samples using two different grades of carbon black.

The fired porosity of the cathode samples is surprisingly high compared to that of the LCM support. One possible explanation for this is that the YSZ is not fully sintering in the samples without nanoalumina sintering aid, even though YSZ densification is possible at 1300°C. To confirm this, a sample with 1 wt% nanoalumina on weight of YSZ was formulated and fired. The result is also shown in Figure 4.18. Indeed, there is further densification in this sample, though still the final porosity is higher than expected from experience with the LCM. This is evidence that the firing program used is well-designed: with the help of a sintering aid, it can barely densify the YSZ components without removing desirable porosity from the LCM components. Lack of densification of the cathode is desirable because the performance of the cell does not depend upon the density of the YSZ in the cathode, as it does the YSZ in the electrolyte.

The final cathode formulation was tweaked to use less PVA binder in order to reduce viscosity, and to use Regal 250R as powdered carbon blacks are more common and available. The formulation is described in Table 4.5.

Table 4.5: Final cathode slurry formulation.

	wt %
LCM	13.68%
YSZ	13.68%
Dolapix CE-64	2.26%
Carbon black	11.32%
PVA	0.73%
Water	58.35%

4.3.4 YSZ electrolyte

The general form of the YSZ slurry is given in Table 4.6. The material choice and dosage of Dolapix CE-64 is discussed in Section 4.3.1. The PVA binder amount is held at 2 wt % on weight of water to impart some viscosity. The nanoalumina is held at about 1 wt % on weight of YSZ. The purpose of the nanoalumina is to decrease the temperature at which the YSZ sinters. This material choice and dosage is selected to mimic Yoon's 2008 work. The nanoalumina powder was obtained from Sigma-Aldrich (part number 544833).

Table 4.6: General formulation of the YSZ electrolyte slurry.

	wt %
YSZ	30-60%
Dolapix CE-64	0.33%
PVA	1.17%
Nanoalumina	0.35%
Water	68-38%

It is important to use a sintering aid in the YSZ formulation because we desire to fully densify the electrolyte without over-sintering the LCM support or the LCM/YSZ cathode. Over-sintering of the support or the cathode would be problematic because it would reduce the oxygen flow to the cathode, limiting the cell's performance. This topic is discussed further in Section 1.2.2.

Since electrolyte density is critical to cell performance as well as mechanical integrity, effort was made to characterize the porosity electrolyte material by the Archimedes method. Initially, small samples were slip cast as was done with the cathode slurry. However, the electrolyte slurry stuck to the plaster mold and could not be removed for characterization.

Next, the electrolyte slurry was tape-cast at a wet thickness of 0.005 in. Excess binder was added to the formulation to ensure that it would release from the polyethylene substrate. It was anticipated that if the fired porosity was less than or equal to the dry volume percentage of binder, it could be assumed that a formulation with less binder would sinter to full density. Unfortunately, the film wrinkled during sintering to the degree that Archimedes density measurement was impossible. The formulation used here is given in Table 4.7 and the tape casting process is described in Figure 4.19.

Table 4.7: Formulation used for tape-casting the electrolyte slurry.

	wt %
YSZ	28.75%
Dolapix CE-64	1.44%
PVA	8.21%
Water	61.60%



Figure 4.19: Left: the setup used to tape cast the YSZ slurry. Right: The dried YSZ film. This technique was a failed attempt to characterize the porosity of the electrolyte layer without coating it on a complete cell, but was not used in fabrication of the titular structure.

The conclusion was that the electrolyte layer must be characterized in situ. To that end, a YSZ slurry at 14 vol % total solids was prepared. A support was casted, dried, and the cathode and electrolyte layers were dip coated onto it and dried. This electrolyte slurry produced a very thin coating, so it was dipped and dried twice. The resulting structure was fired and then imaged in cross-section in an SEM. The images gathered are shown in Figure 4.20 and Figure 4.21.

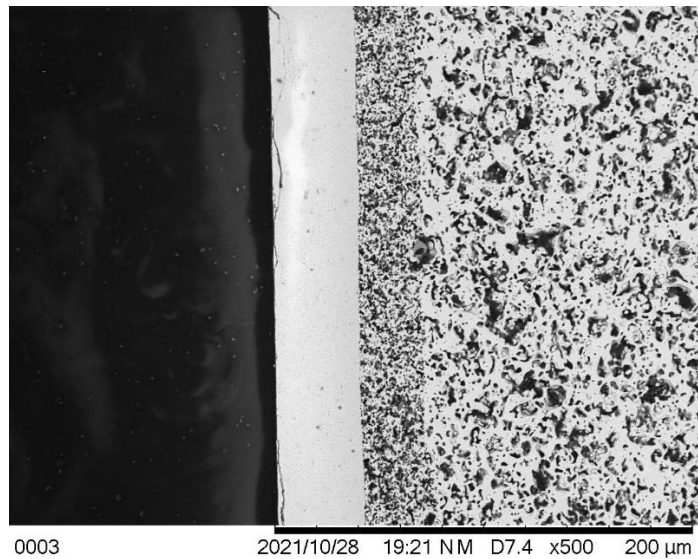


Figure 4.20: SEM micrograph showing the thickness of the electrolyte at this point in development to be about 40 μm .

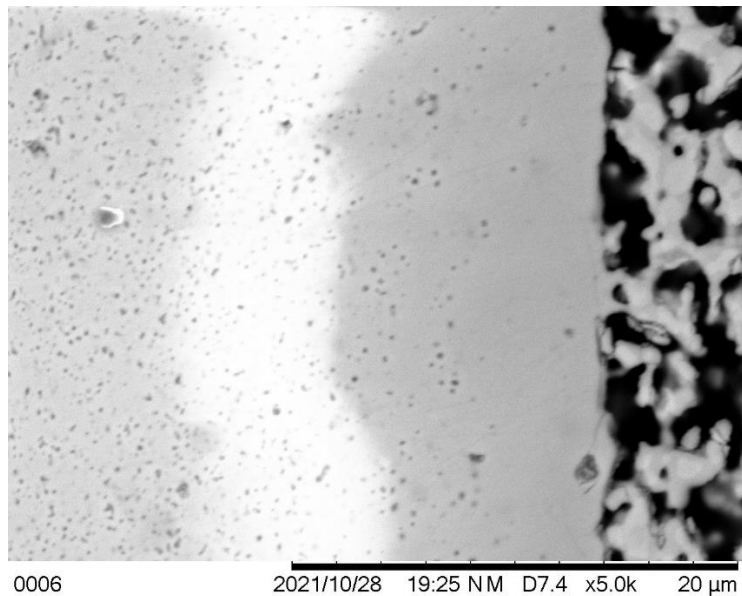


Figure 4.21: SEM micrograph showing almost full density of the YSZ electrolyte layer.

The target thickness for the electrolyte layer was 20 μm . Yoon's 2008 work showed good performance from planar SOFC cells with 15 μm YSZ electrolytes; it was decided to target slightly thicker for this application due to the harsh environment of liquid alloy into which this coating will be submerged. Figure 4.20 shows that two dips of this electrolyte slurry gave a thickness of 40 μm . Figure 4.21 shows the two distinct layers of YSZ and a band between them where the first coating,

which had dried, mixed with the second coating when it was applied. It also shows that the electrolyte is almost fully dense after being sintered with firing program #2, which is described in Figure 3.7.

One option would be to use only one dip of this slurry to achieve a 20 μ m thickness. However, the slurry settled quickly due to its low viscosity. The solids loading of the slurry was increased in an attempt to produce a more stable slurry without dramatically increasing the thickness of the electrolyte. YSZ slurries with total solids loadings of 20 and 26 vol % were formulated. The rheologies of the YSZ slurries at 14, 20, and 26 vol % solids are shown in Figure 4.22. The expected trend of viscosity increasing with solids loading is seen. Interestingly, no thixotropy is seen. Since viscosity increases with solids loading, wet film thickness will increase as well. So the increase in thickness of the dry electrolyte film will be of the order 2, because a thicker wet layer is deposited, and the film loses less material upon drying.

The increase in viscosity was marginally successful at preventing settling; however, each YSZ slurry tested settled noticeably after a few days.

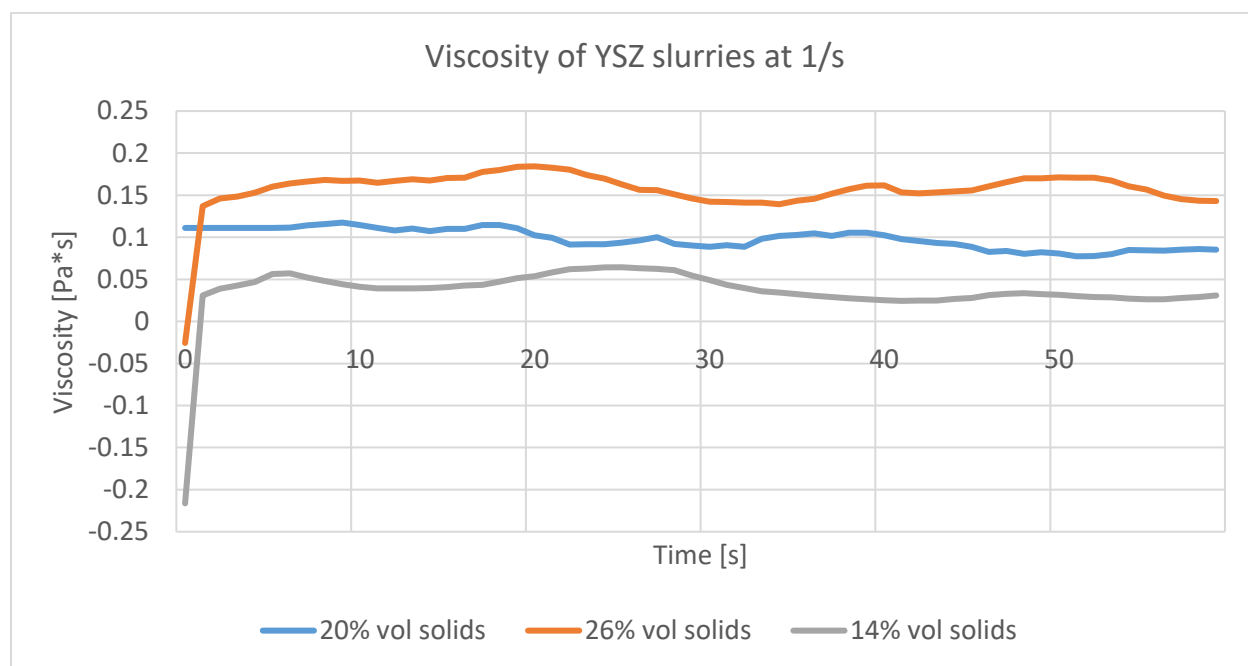


Figure 4.22: Rheology of YSZ slurries at various solids loadings. As expected, higher solids loading corresponds to higher viscosity.

These slurries were similarly applied (as a single dip) to support-cathode structures and imaged via SEM. Figure 4.23 shows the electrolyte layer produced by one dip of a YSZ slurry of 20 vol % solids; Figure 4.24 shows the electrolyte layer produced by one dip of a YSZ slurry of 26 vol % solids. Both figures show cracks in the electrolyte layer, caused during sintering, as the firing process development work described in Section 4.5 was still in progress.

Unfortunately, both of these thicknesses exceeded the target of 20 μ m, and the slurries which produced them did not give much benefit in settling resistance. Therefore, a one dip procedure with the initial solids loading of 14 volume % was accepted as optimal for this work. The final formulation is given in Table 4.8.

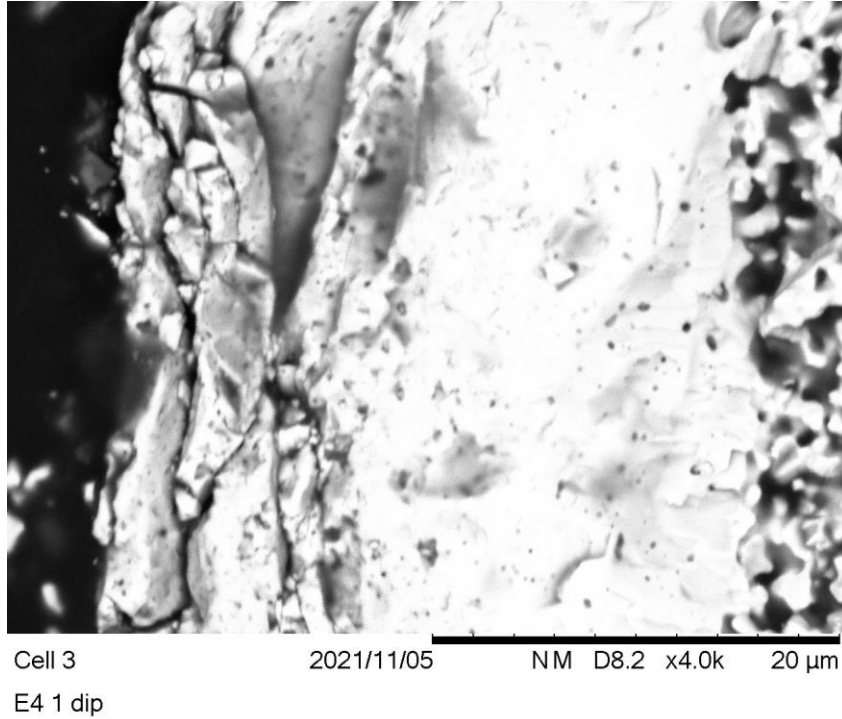
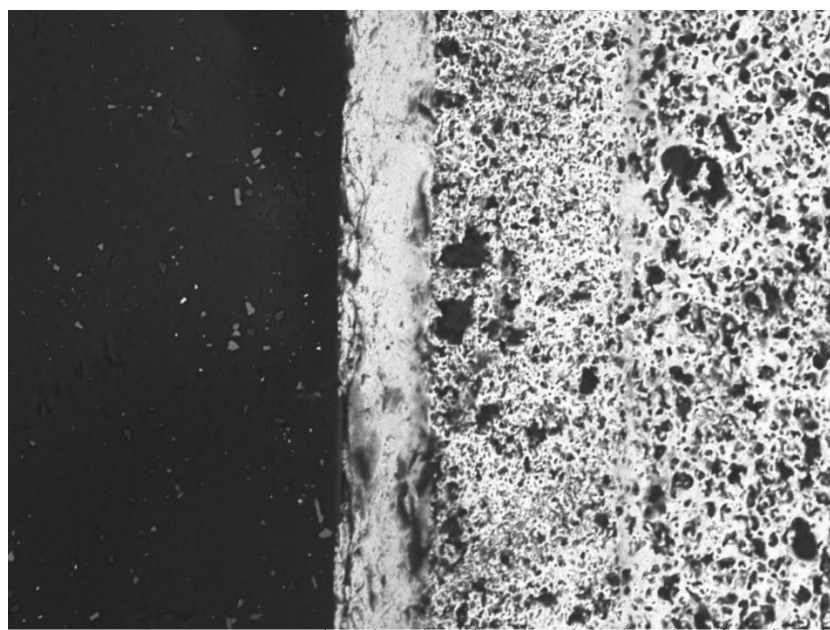


Figure 4.23: SEM micrograph showing the thickness of the electrolyte layer to be about 30 μ m. Cracks are present because the firing process had yet to be fully developed.



Cell 6
E5 1 dip
2021/11/05 NM D7.6 x500 200 μm

Figure 4.24: SEM micrograph showing the thickness of the electrolyte layer to be about 40μm. Cracks are present because the firing process had yet to be fully developed.

Table 4.8: Final formulation for the YSZ electrolyte slurry.

	wt %
YSZ	39.65%
Dolapix CE-64	0.33%
PVA	1.17%
Nanoalumina	0.35%
Water	58.49%

4.4 Dip coating of cathode and electrolyte

Initially, unfired LCM support samples were hung from small alligator clips and the coating bath was raised around them, as shown in Figure 4.25.



Figure 4.25: An unfired LCM support sample being dip coated. The sample is hung from a holder and the coating bath is raised around it. This method was problematic.

This method had two issues. First, the alligator clips put too much pressure on the unfired LCM part, causing damage. Second, the buoyancy of the support prevented the coating from reaching all the way up the wall of the part as desired.

These problems were solved by moving to a new process. In this process, the LCM support is first dried in the oven at 50-75°C for about 30 min. Then, it is held by the flange with tweezers and dipped into the coating bath before being hung by the flange from a holder. This process is described by Figure 4.26.



Figure 4.26: The improved dip coating process: the LCM support is dried, then dipped and dried by its flange.

4.5 Firing

Initially it was not clear if it would be possible to co-fire the three-layer composite structure without it cracking due to differential shrinkages between layers. As discussed in Sections 4.3.2 and 4.3.3, neither the LCM support nor the LCM/YSZ cathode densified significantly upon successive firings, so there was full latitude in designing the firing process. On one extreme, all three layers could be co-fired; on the other, the part could be sintered three times: first as the support only, then after the cathode coating was applied, then again after the electrolyte coating was applied. The possibilities are shown in Figure 4.27.

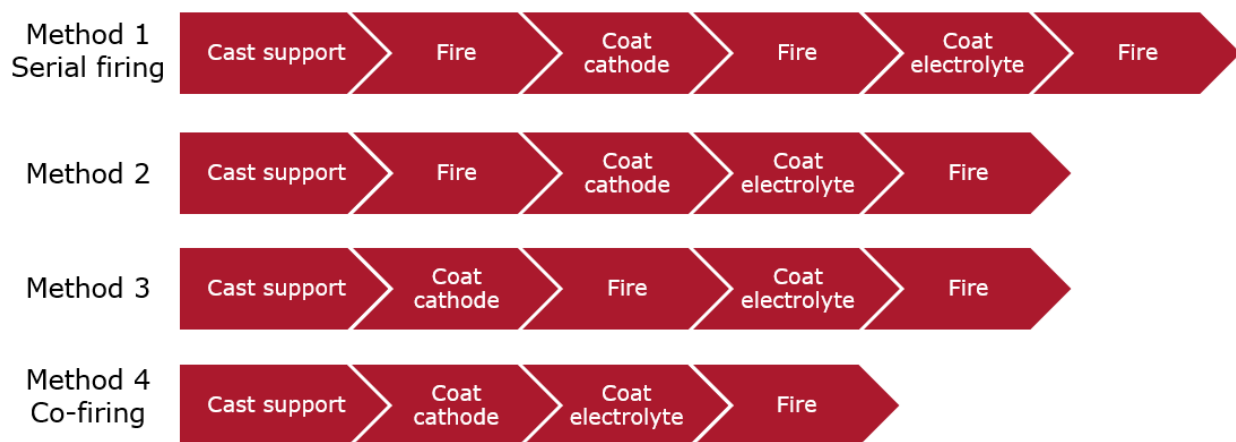


Figure 4.27: Firing method possibilities. Method 4 was selected because it produced prototypes without cracks in any layer and is the simplest to implement in manufacturing.

Method 1 represents complete serial firing, where the structure is fired after the formation of each layer. In this method, the support would experience 3 firing cycles. Method 4 represents complete co-firing, where all three layers are formed and then sintered in a single firing cycle. Methods 2 and 3 are intermediate methods, where some layers are serially fired and some are co-fired. It was important to test each method because the shrinkage due to sintering of each layer was unknown, and as discussed in Section 1.3.4, it is critical to cell integrity to minimize the difference in shrinkage between layers.

Methods 1 and 3 failed when the structure was fired with the cathode layer exposed. In both cases, the cathode layer cracked and peeled off of the support, producing the structure shown in Figure 4.28.



Figure 4.28: The result of firing methods 1 and 3. Left: A cathode layer which has cracked during firing. Right: the inside view of the same sample, showing a support with no significant cracking.

Since both methods 1 and 3 failed in the same way, this indicates that there is not a large difference in stress due to shrinking at the sintered support-green cathode interface versus at the green support-green cathode interface. However, it does indicate that the cathode layer is unstable if exposed during sintering.

Method 2 produced a prototype with a cracked electrolyte later, pictured in Figure 4.29.

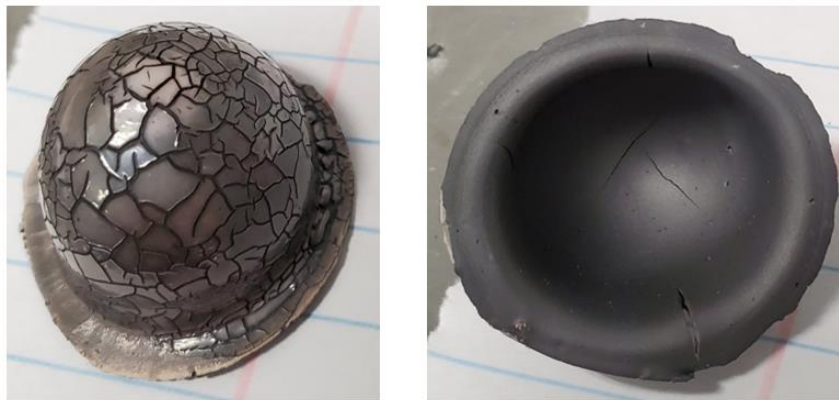


Figure 4.29: The result of firing method 2. Left: an electrolyte layer which has cracked during firing. Right: the inside view of the same sample, showing a support with no significant cracking.

This result shows that there is likely a significant difference in shrinkage during sintering between the already-sintered support and the green electrolyte layer.

Firing method 4, which represents full co-firing, yielded the best results. Figure 4.30 shows that neither the inside nor the outside developed significant cracking. The electrolyte layer does show some pinhole defects, but these are due to entrained air in the slurry, not cracking from differential shrinkage between layers during sintering.



Figure 4.30: Left: an uncracked electrolyte layer. Pinhole defects in the electrolyte are due to entrained air in the slurry. This is the result of firing method 4. Right: the inside of the same sample, showing no cracks in the support.

Firing method 4, complete co-firing, was accepted as the optimal firing method for producing this structure. First, this method gave the best quality of sintered part. In addition, this method is the least time-consuming and simplest of the possible methods. This is important because manufacturability is one of the few remaining hurdles in the path towards commercializing DCFC technology.

4.6 Scale-up

Attempts were made to produce slip-casted support structures approximately 7" in length to further develop the manufacturability of the technology and for easier cell testing.

Initially, a capped 3" polyvinyl (PVC) pipe was used as a case mold for a larger plaster mold. Plaster was prepared according to the procedure in Section 3.4 and poured into the case mold. A custom-machined mandrel, seen in Figure 4.31, was inserted into the plaster. The mandrel included a flange so that it was supported by the edge of the PVC pipe. The mandrel was removed when the plaster had dried, producing a mold with a long void.

The cap was cemented to the pipe in the first iteration of the case mold, so the dry plaster mold could not be removed. This prevented the plaster, and later the LCM support, from drying in a timely fashion.



Figure 4.31: Mandrel used for producing scaled-up plaster molds. The mandrel was inserted into wet plaster and removed when the plaster dried.

The next iteration of the case mold was a three-part system, consisting of a 3" PVC pipe cut in half along its long axis and a cap. The two halves of the pipe were fitted together inside the cap and held in place with hose clamps, then filled with plaster. The same mandrel was inserted and the plaster was left to dry. The improved case mold and the plaster mold it was used to produce are pictured in Figure 4.32.



Figure 4.32: Three-part case mold and plaster mold produced with it.

Attempts to cast an LCM support in this mold were frustrated. The formulation from Table 4.2 and the procedure described in Section 3.4 was used with a casting time of 5 minutes, as these

parameters had produced small-scale samples without cracks. Unfortunately, as can be seen in Figure 4.33, the large samples cracked while drying the mold.



Figure 4.33: Samples casted in the scaled-up mold. They cracked while drying in the mold.

The issue of cracking in the mold had been encountered with the small slip-casted samples, and was solved by using only freshly mixed LCM slurry. Doing so did not prevent cracking in the large samples. It was further hypothesized that the flange at the top of the cast was causing the issue. Since the larger samples would shrink much more along their long axis during drying, and the flange would hold the top of the cast in place, the stress between gravity and shrinkage could cause cracking. To explore this, a sample which did not completely fill the mold (and so had no flange) was cast. Though it was comparably free to move during drying, it cracked as well. Finally, it was hypothesized that the cast was simply too thin to withstand the stress from shrinking during drying. A sample was cast for 15 minutes (three times as long as usual), but this too cracked in the mold.

Unfortunately, a scaled-up structure is out of the scope of this work. Suggestions on producing a scaled-up are discussed in Section 7.

5 Results

5.1 Composite characterization by SEM

Three full support-cathode-electrolyte structures were characterized by cross-sectional SEM. They are described in Table 5.1.

Table 5.1: Summary of samples characterized by SEM cross-section.

Sample identifier	Support		Cathode layer		Electrolyte layer	
	Pore former content [vol %]	Intended average pore diameter [μm]	Pore former content [vol %]	Intended average pore diameter [μm]	Solids loading [vol%]	Thickness [μm]
Cell 1	50%	20	40%	5	14%	20*
Cell 3					20%	30
Cell 6					26%	40

*This sample was dipped in the electrolyte slurry twice, so the reported number is half the measured thickness.

The goals of the SEM analysis were: 1) to confirm the approximate porosity and pore diameter for the support and cathode, 2) to confirm that the electrolyte layer was fully dense, and 3) to develop a relationship between solids content and dry coating thickness for the electrolyte layer.

Figure 5.1, Figure 5.2, and Figure 5.3 display the images of Cell 1, Cell 3, and Cell 6, respectively.

Much is learned from these images. First and foremost, they show that the intended structure has been achieved. A coarsely porous support has been coated with a finely porous cathode and a fully dense electrolyte. To emphasize their similarity, the schematic of the intended structure is reproduced side-by-side with the produced structure in Figure 5.4. Second, the images confirm that the porosity in both the support and the cathode is open and will allow oxygen gas to be ionized in at the cathode-air interface for good cell performance. Third, the approximate average pore size for both the support and the cathode are confirmed to match the targets of $20\mu\text{m}$ and $5\mu\text{m}$, respectively. Fourth, the electrolyte is shown to be almost fully dense. Cracks are present in Figure 5.2c and Figure 5.3c, but these are the result of shrinking mismatch during firing, not incomplete sintering. An insignificant amount of closed porosity, which is likely the result of the binder in the electrolyte formulation, can be seen in Figure 5.1c. A small amount of binder is necessary in the formulation to increase viscosity and is not expected to degrade cell performance. Fifth, the thickness of the support is confirmed to match the target of 2mm . Sixth, the thickness of the cathode layer is confirmed to match the target of $40\mu\text{m}$. Finally, the relationship between electrolyte solids content and dry thickness is shown to be linear, and 14 vol% solids is shown to achieve the target thickness of $20\mu\text{m}$.

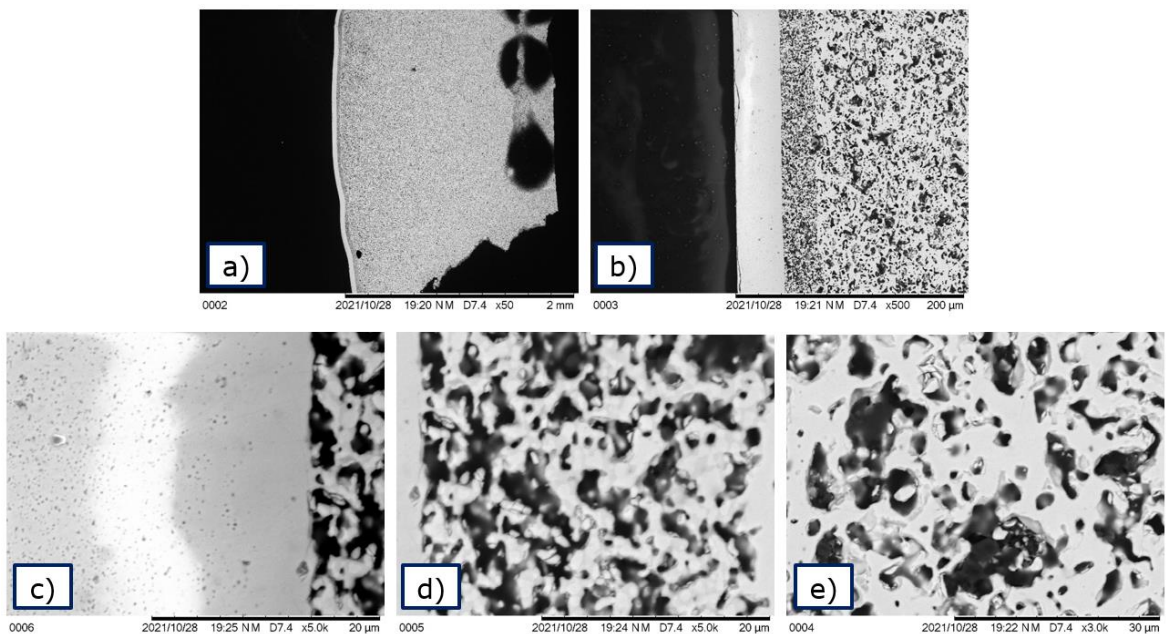


Figure 5.1: SEM images of Cell 1. a) Low-magnification view showing all 3 layers and thickness of support. b) View showing all 3 layers distinctly, and thicknesses of cathode and electrolyte. c) High-magnification view showing low porosity in electrolyte. d) High-magnification view showing porosity in the cathode. e) High-magnification view showing porosity in the support.

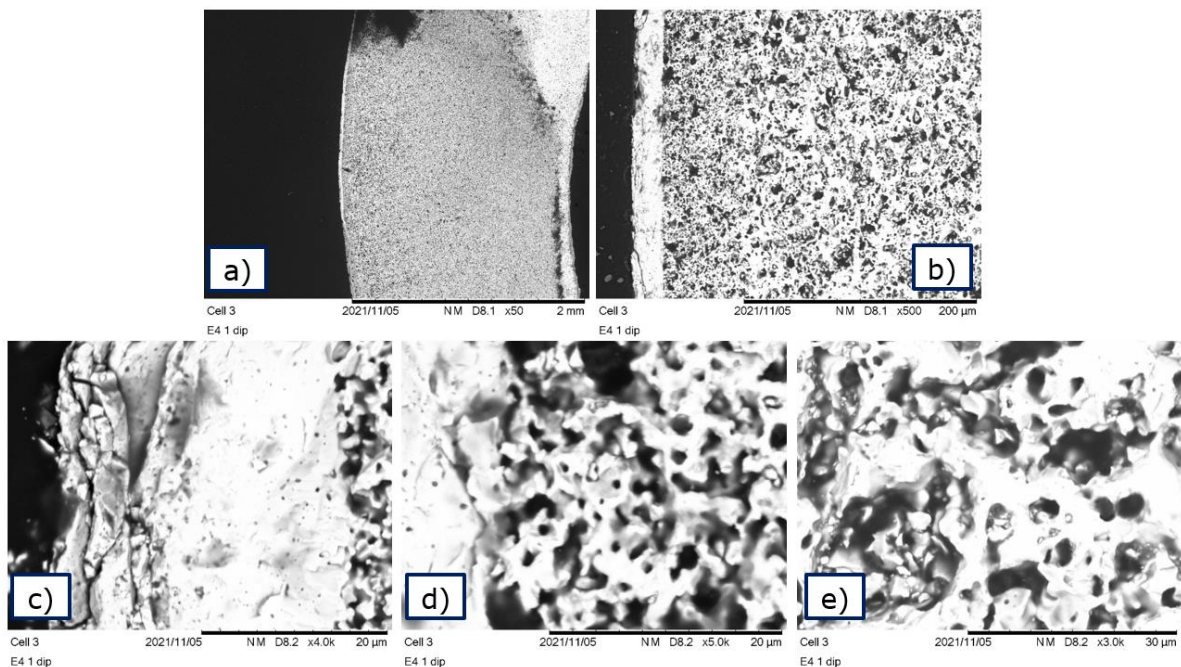


Figure 5.2: SEM images of Cell 3. a) Low-magnification view showing all 3 layers and thickness of support. b) View showing all 3 layers distinctly, and thicknesses of cathode and electrolyte. c) High-magnification view showing lack of porosity in electrolyte. d) High-magnification view showing porosity in the cathode. e) High-magnification view showing porosity in the support.

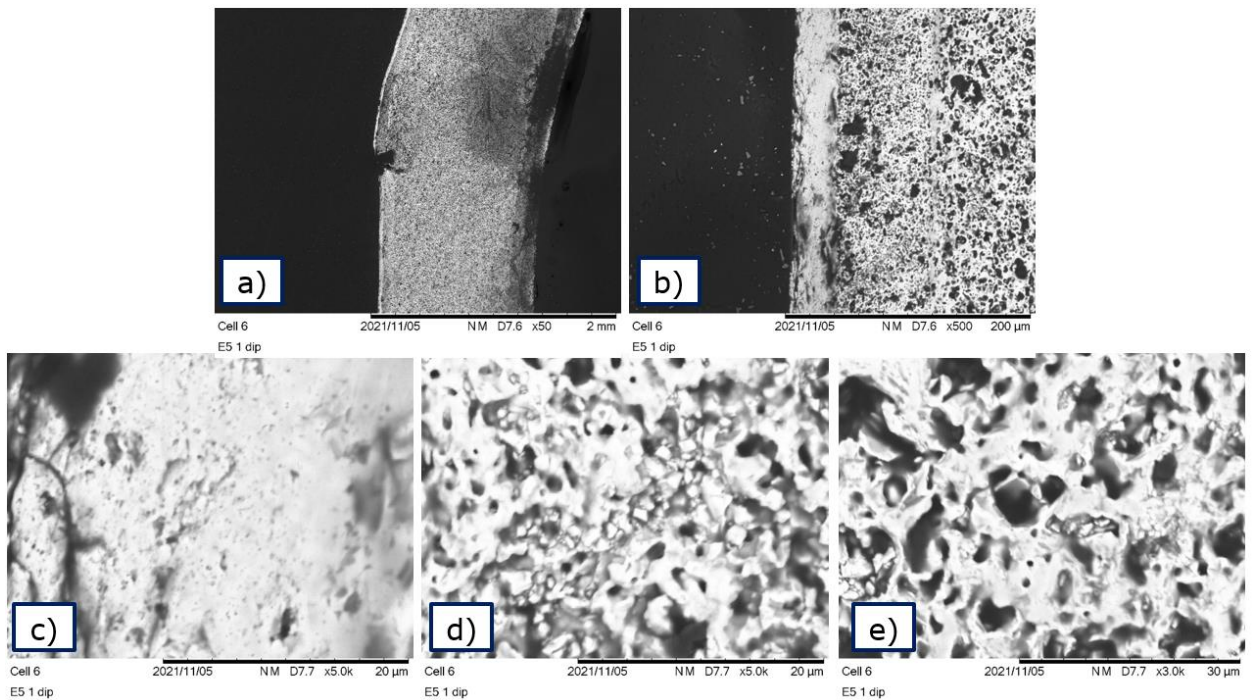


Figure 5.3: SEM images of Cell 6. a) Low-magnification view showing all 3 layers and thickness of support. b) View showing all 3 layers distinctly, and thicknesses of cathode and electrolyte. c) High-magnification view showing lack of porosity in electrolyte. d) High-magnification view showing porosity in the cathode. e) High-magnification view showing porosity in the support.

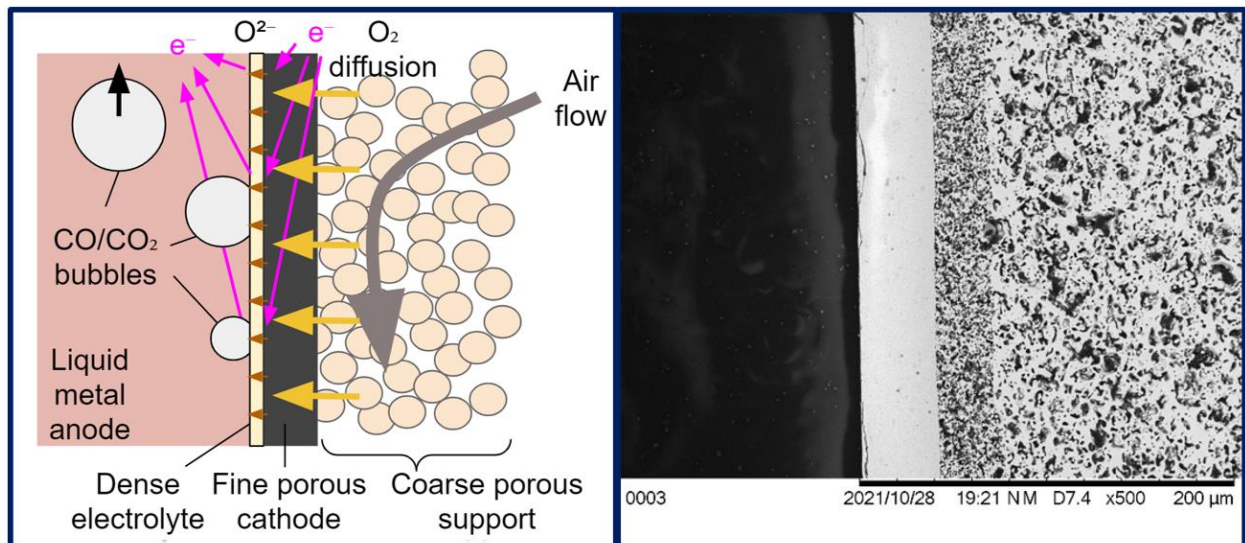


Figure 5.4: Left: Schematic of the intended structure of the support-cathode-electrolyte structure. Right: SEM image of the produced structure.

5.2 Cell testing

Results of cell testing were mixed. The apparatus operated as intended mechanically and thermally; however, the measured voltage data is problematic.

5.2.1 Mechanical and Thermal

The cathode-electrolyte structure, which is the focus of this work, maintained mechanical integrity throughout testing. Sensitivity to thermal shock was not an issue for the developed structure. A visual comparison of the structure before and after testing at above 1000°C for about 5 hours is given in Figure 5.5.



Figure 5.5: Left: cathode-electrolyte structure before testing. Right: The same structure after testing.

On the macro scale, the primary difference between the appearance of the structure before and after is that after testing, it is partially coated with solidified anode alloy. This confirms that the electrolyte and anode were in good electrical contact during testing. The ceramic cement maintained adhesion and gas-tight sealing between the structure and the mullite support tube. While there is some discoloration of the electrolyte, there appears not to be significant degradation after about 5 hours of operation at high temperature. The pinhole defects seen in the before image are perhaps aggravated during testing. These can be prevented by using a degassing procedure before dip coating, as discussed in Section 7.

To discover any differences on the micro scale, two used cathode-electrolyte structures were cross-sectioned and examined by SEM. A structure which was operated at 1000°C for about 1.5 hours is

detailed in Figure 5.6. A structure which was operated between 1000°C and 1100°C for about 5 hours is detailed in Figure 5.7.

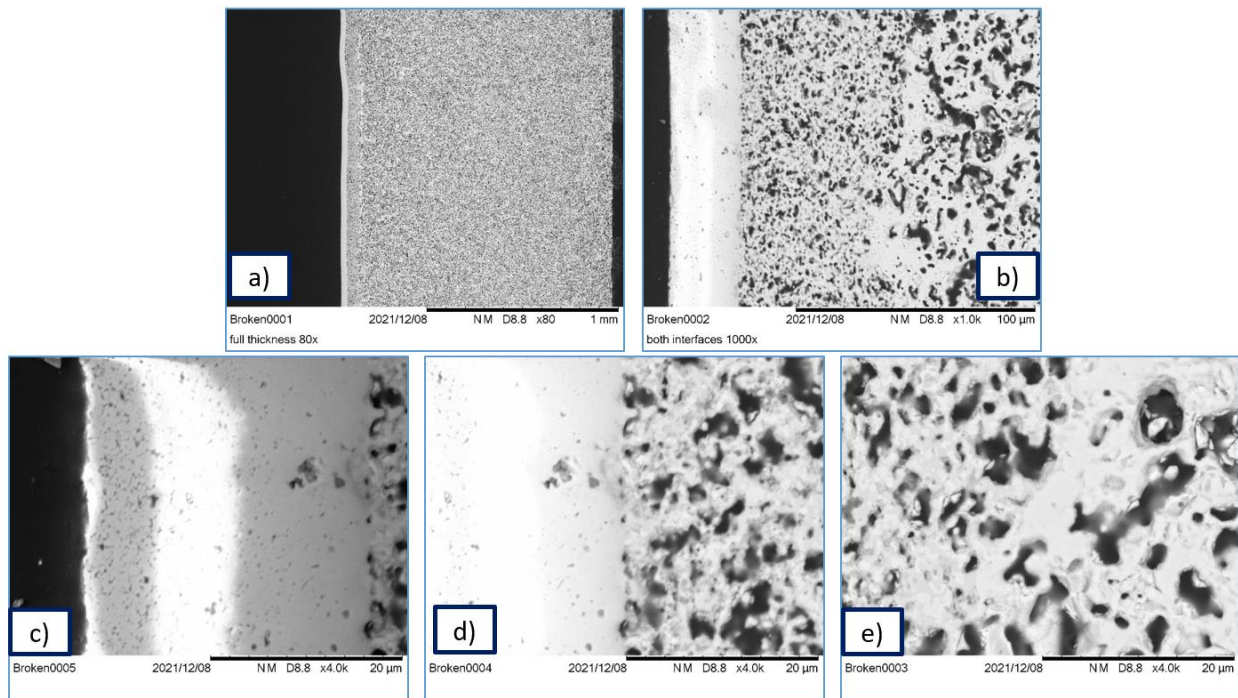


Figure 5.6: SEM cross-sections of a cathode-electrolyte structure which was operated at 1000°C for about 1.5 hours. a) The total thickness of the structure. b) The electrolyte-cathode and cathode-support interfaces. c) The outer edge of the electrolyte. d) The electrolyte-cathode interface. e) The cathode-support interface.

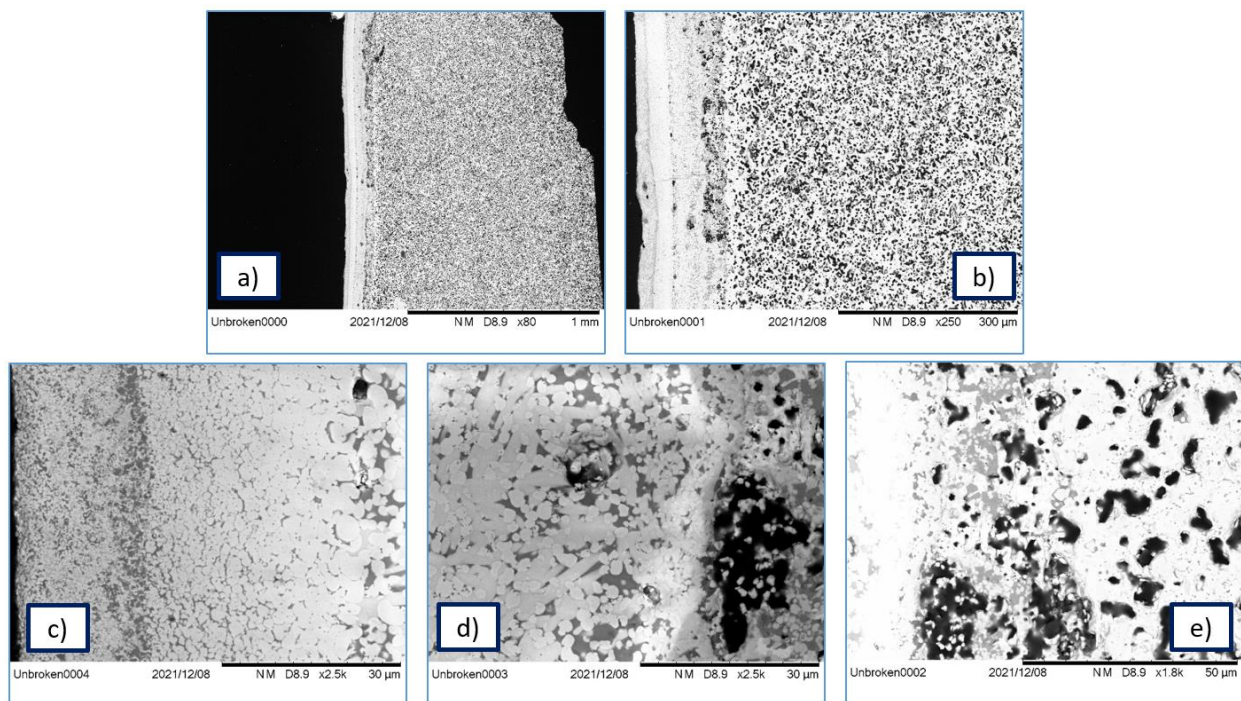


Figure 5.7: SEM cross-sections of a cathode-electrolyte structure which was operated at 1000°C-1100°C for about 5 hours. a) The total thickness of the structure. b) The electrolyte-cathode and cathode-support interfaces. c) The outer edge of the electrolyte. d) The electrolyte-cathode interface. e) The cathode-support interface.

Figure 5.6 and Figure 5.7 may be compared to the right-hand panel of Figure 5.4, which is a cross-section of an unused structure. Differences between the unused structure and the structure which was operated for 1.5 hours are minimal if any. There is perhaps some slight roughness in the outer edge of the structure operated for 1.5 hours. The structure which was operated for 5 hours shows some noticeable differences on the micro scale. Most significant is that the cathode-electrolyte interface is less sharply defined. This may be the result of reaction between the YSZ and LCM, or diffusion of the calcium dopant from the lanthanum manganite into the zirconia. Finally, a slight roughening of the outer edge of the electrolyte is also seen. Further study is required to determine if or how these differences in microstructure affect the performance of the cell over time.

Complete melting was achieved in the anode alloy, shown post-testing in Figure 5.8. This is an improvement from Faria’s 2021 work, and likely the result of the pre-melting procedure described in Section 3.9.1.



Figure 5.8: Alloy 1 post-testing. Complete melting was achieved.

Finally, the graphite rod used as the anode current collector was verified to be in good electrical contact with the anode because it too was coated in metal after testing. The alloy-coated rod is shown in Figure 5.9.



Figure 5.9: The anode current collector post-testing.

5.2.2 Electrical

First, the open circuit voltage (OCV) of the system was measured at 1000°C. OCV measurements over 30 minutes of operation are described in Figure 5.10.

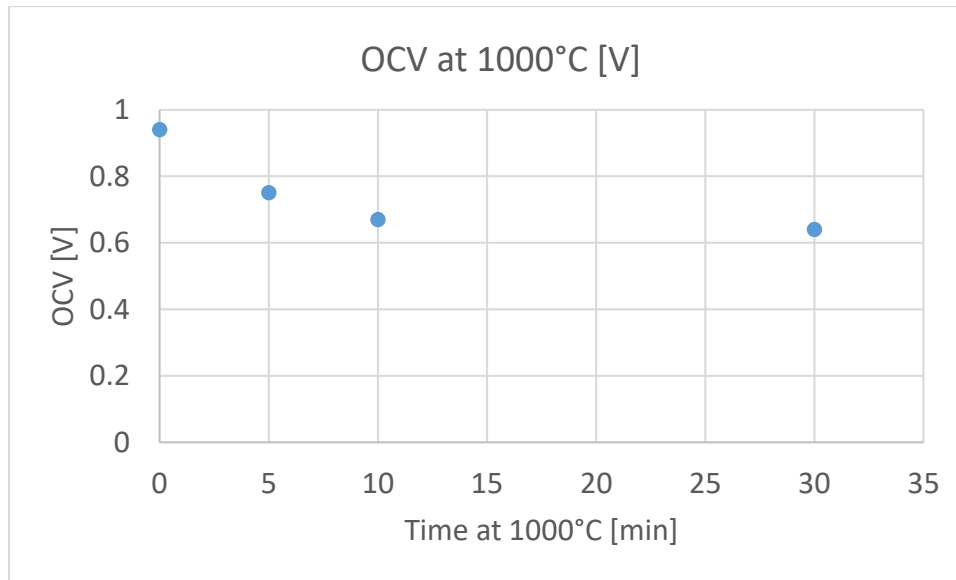


Figure 5.10: OCV measurements over 30 minutes of operation at 1000°C.

These data are important because they establish that the cathode-electrolyte structure is maintaining structural integrity. The electrolyte coating provides a robust enough separator that the circuit does not short and that the injected oxygen gas does not leak out.

E_{th} for this cell at 1000°C and 1bar was calculated by Faria to be 1.35V, so it is encouraging to reach 0.98V in this work. The drop in OCV over 10 minutes of operation is likely due to the carbon in contact with the electrolyte being consumed during operation, which is evidence of the cell functioning as intended. As carbon is consumed in the anode in contact with the electrolyte, the activity of carbon in this region decreases. Section 1.2.1 describes how a decrease in overall voltage should be expected from a decrease in carbon activity. The cell was disconnected between the 10- and 30-minute measurements; the fact that OCV remains unchanged is further evidence of carbon being consumed during cell operation, and this process pausing when the cell is disconnected.

It is helpful to compare this OCV data against Faria's 2021 results, which achieved only about 0.4V with the same experimental setup except for a 2mm thick YSZ tube in place of the developed structure. Juxtaposing that work with the present isolates the significant increase in OCV as the result of the developed structure alone.

6 Conclusions

A tubular support-cathode-electrolyte structure for use in a DCFC with liquid metal anode has been developed.

The support, which also functions as the current collector, is made of LCM and has a porosity of about 35% 20µm pores. It is fabricated to a thickness of 2mm by slip casting with a casting time of 5 minutes. The porosity could not be increased because doing so compromised the mechanical

integrity of the support, resulting in cracked casts. The viscosity of the support slurry had to be limited to about 2000cP to ensure good draining from the mold during slip casting. Scaling up of the structure will require slip-casting process modifications to ensure uniform drying or formulation adjustments to improve green strength.

The cathode layer is made of an equal mass blend of LCM and YSZ. This ensures that its shrinkage upon sintering and thermal expansion coefficient will be compatible with those of both the support and the electrolyte, thus preventing delamination during fabrication or operation. It has a fired porosity of about 35% 5 μ m pores and a thickness of about 40 μ m. It is applied to the support by dip coating. The electrolyte is made of zirconia doped with 8 mol % yttria to maximize oxygen ion vacancies. It is applied to the structure by dip coating on top of the dried cathode layer. It has a thickness of about 20 μ m and a porosity of nearly 0%.

Although aqueous systems are becoming more popular, most DCFC technology uses at least some organic solvent. The developed formulations advance the sustainability of the technology by using none.

In addition, this work moves DCFC technology closer to mass manufacturability by utilizing slip casting which is a relatively inexpensive and scalable process.

The structure is co-fired for 2 hours at 1300°C. It is fired horizontally to maintain even sintering throughout its length. Firing the structure with the cathode layer exposed resulted in delamination and cracking of the cathode layer. Firing the support before coating the cathode or electrolyte produced a cracked electrolyte layer due to differential shrinkages between layers during sintering.

The results of testing the developed structure in the fuel cell are encouraging from a mechanical perspective. The cathode-electrolyte structure did not display damage or significant degradation after about 5 hours in contact with the molten anode at about 1000°C. A promising result from electrical testing is that the initial open-circuit voltage nearly reaches the theoretically-predicted value and decreases as the cell operates.

7 Future Work

Immediate next steps for the work include collecting power density and voltage versus current density data at various temperatures, thereby characterizing the cell's performance. This data should be gathered before further work is conducted on the cathode-electrolyte structure, because it is necessary to have a baseline upon which to improve. Suggestions for collecting reliable performance data include using a platinum wire mesh to improve the cathode electrical contact, using a potentiostat for measurement, and using separate electrical leads for operation and measurement.

With regard to the cathode-electrolyte structure, future work is suggested in the areas of scale-up, cell performance, and manufacturability.

To scale-up the LCM support slip casting process, reformulation is likely required. If the cracking is due to drying too quickly or uneven drying, the mold could be wetted before casting. Failing this, the green strength of the cast must be increased to withstand the stresses generated during drying. Amount and type of binder could be adjusted, so long as it does not cause the cast to stick to the mold and does not increase viscosity to the point of poor draining. Another way to do this is to adjust the amount and type of pore former. It is possible that the ceiling for 20 μ m porosity identified in Section 4.3.2 decreases as the cast dimensions increase. A pore former with lower particle size, or less of the same pore former could be used. This is recommended as a last resort, because it will decrease cell performance by decreasing oxygen delivery rate to the cathode.

In terms of increased cell performance, it may be possible to increase the porosity of the support by using a bimodal pore former, such as a blend of the 20 μ m cellulose and 5 μ m carbon black used in this work. As discussed in Section 4.3.2, the limit of formulated porosity from 20 μ m cellulose was 50%. Adding small interstitial pores between the larger pores may increase the total porosity (and thereby oxygen delivery rate) without compromising the mechanical integrity of the support. Further, it may be possible to decrease the thickness of the support by decreasing the casting time. This would also reduce the pressure drop of the gas as it is delivered to the cathode. This may also be a strategy to allow larger casts with adequate green strength.

Regarding manufacturability, pinholes were a common defect in the cathode and electrolyte coatings. Surfactant loading should be decreased where possible without allowing particle agglomeration, and a degassing step should be implemented during slurry preparation. In addition, a rheology modifier could be added to the slurries to increase viscosity and prevent settling. The increased viscosity must be checked against good drainage during slip casting of the LCM slurry, and against optimal coating thickness of the cathode and electrolyte slurries. In the same vein, the stability of the YSZ slurry could be increased with an alternate ionic dispersant or a steric dispersant. It would be desirable to screen ionic dispersants which could increase the magnitude of the ZP to at least 40 mV to prevent settling of the slurry. A smaller particle size of YSZ powder may have the same effect.

A topic that touches on both performance and manufacturability is density of the electrolyte. Complete densification was not achieved, and voids in the electrolyte will retard oxygen ion transport, reducing performance. Higher sintering temperatures or longer sintering times may be explored, so long as they do not over-sinter the support or cathode, reducing oxygen delivery rate. Alternatively, a bimodal grade of YSZ powder could be used to achieve tighter packing between particles. Tighter packing translates to higher green density and less of a burden on the sintering process for densification.

8 References

Bai, Y., Liu, J., Gao, H., & Jin, C. (2009). Dip coating technique in fabrication of cone-shaped anode-supported solid oxide fuel cells. *Journal of alloys and compounds*, 480(2), 554-557.

-
- Bai, Yaohui, et al. "Direct carbon solid oxide fuel cell—a potential high performance battery." *international journal of hydrogen energy* 36.15 (2011): 9189-9194.
- Colet Lagrille, M. A. (2013). *Carbon-Air Fuel Cells with Molten Tin Anodes*. Doctoral thesis. Imperial College of London.
- EIA (2020). *Electricity in the United States*. U.S. Energy Information Administration. <https://www.eia.gov/energyexplained/electricity/electricity-in-the-us.php>
- EPA (2019). *Sources of Greenhouse Gas Emissions*. EPA. <https://www.epa.gov/ghgemissions/sources-greenhouse-gas-emissions>
- Faria, Christian. (2021). *High-Efficiency High Power Direct Carbon Fuel Cell*. Master's Thesis. Worcester Polytechnic Institute.
- Florides, G. A., & Christodoulides, P. (2009). Global warming and carbon dioxide through sciences. *Environment international*, 35(2), 390-401.
- Gans, Adrien, et al. "Dip-coating of suspensions." *Soft matter* 15.2 (2019): 252-261.
- Giddey, S., Badwal, S. P. S., Kulkarni, A., & Munnings, C. (2012). A comprehensive review of direct carbon fuel cell technology. *Progress in Energy and Combustion Science*, 38(3), 360-399.
- Giddey, S., Kulkarni, A., Munnings, C., & Badwal, S. P. S. (2014). Performance evaluation of a tubular direct carbon fuel cell operating in a packed bed of carbon. *Energy*, 68, 538-547.
- Grahame, D. C. (1947). The electrical double layer and the theory of electrocapillarity. *Chemical reviews*, 41(3), 441-501.
- Huang, K., & Singhal, S. C. (2013). Cathode-supported tubular solid oxide fuel cell technology: A critical review. *Journal of power sources*, 237, 84-97.
- Ido, A., & Kawase, M. (2020). Development of a tubular molten carbonate direct carbon fuel cell and basic cell performance. *Journal of Power Sources*, 449, 227483.
- IPCC (2014). *Climate Change 2014: Mitigation of Climate Change. Contribution of Working Group III to the Fifth Assessment Report of the Intergovernmental Panel on Climate Change*. Cambridge University Press.
- Jacques, W. W. (1896). Electricity direct from coal. *Harper's Magazine*, 94, 144-150.
- Jiang, S. P. (2008). Development of lanthanum strontium manganite perovskite cathode materials of solid oxide fuel cells: a review. *Journal of Materials Science*, 43, 6799-6833.
- Johnson, J. L., Tan, L. K., Suri, P., & German, R. M. (2003). Design guidelines for processing bi-material components via powder-injection molding. *Jom*, 55(10), 30-34.
- Kober, T., Schiffer, H. W., Densing, M., & Panos, E. (2020). Global energy perspectives to 2060—WEC's World Energy Scenarios 2019. *Energy Strategy Reviews*, 31, 100523.

-
- Kouchachvili, L., Geddis, P., & Zhuang, Q. (2021). Direct carbon fuel cell design for continuous operation. *International Journal of Hydrogen Energy*, 46(9), 6792-6802.
- Kumar, Ajeet, and Chandra Kumar Dixit. "Methods for characterization of nanoparticles." *Advances in nanomedicine for the delivery of therapeutic nucleic acids*. Woodhead Publishing, 2017. 43-58.
- L. Landau and B. Levich, "Dragging of a liquid by a moving plate," *Acta Physicochimica URSS*, vol. 17, pp. 42- 54, 1942.
- Largiller, G., Bouvard, D., Carry, C. P., Gabriel, A., Müller, J., & Staab, T. (2012). Deformation and cracking during sintering of bimaterial components processed from ceramic and metal powder mixes. Part I: Experimental investigation. *Mechanics of Materials*, 53, 123-131.
- Pati, Soobhankar (2010). Analysis of solid oxide membrane (SOM) electrolyzer with liquid metal anode. Doctoral thesis. Boston University.
- Reed, James S. (1995) *Principles of Ceramics Processing*. John Wiley & Sons, Inc.
- Ritchie, H., Roser, M. (2020). *Access to Energy*. Our world in data. <https://ourworldindata.org/energy-access>
- Simchi, A. (2006). Densification and microstructural evolution during co-sintering of Ni-base superalloy powders. *Metallurgical and Materials Transactions A*, 37(8), 2549-2557.
- U.S. Department of Energy. *How Gas Turbine Power Plants Work*. Energy.gov. <https://www.energy.gov/fecm/how-gas-turbine-power-plants-work>
- U.S. Department of Energy. *Hydrogen and Fuel Cells*. Energy.gov. <https://www.energy.gov/public-services/vehicles/hydrogen-fuel-cells>
- University of Cambridge. *Fuel Cells (all content)*. <https://www.doitpoms.ac.uk/tlplib/fuel-cells/printall.php>
- ur Rehman, S., Song, R. H., Lee, J. W., Lim, T. H., Park, S. J., & Lee, S. B. (2017). Fabrication and characterization of La_{0.65}Sr_{0.3}MnO_{3-δ}(Y₂O₃)_{0.08}(ZrO₂)_{0.92}/Gd_{0.1}Ce_{0.9}O_{2-δ} tri-composite cathode-supported tubular direct carbon solid oxide fuel cell. *Ceramics International*, 43(1), 1086-1091.
- Wagman, D. D., Kilpatrick, J. E., Taylor, W. J., Pitzer, K. S., & Rossini, F. D. (1945). Heats, free energies, and equilibrium constants of some reactions involving O₂, H₂, H₂O, C, CO, CO₂, and CH₄. *J. Res. Natl. Bur. Stand*, 34(2), 143.
- Wang, Z., Cheng, M., Dong, Y., Zhang, M., & Zhang, H. (2006). Anode-supported SOFC with 1Ce₁₀ScZr modified cathode/electrolyte interface. *Journal of power sources*, 156(2), 306-310.
- Yoon, K. J. (2008) Fabrication process of single step Co-firing SOFC. [Unpublished notes.]
- Yoon, K. J., Gopalan, S., & Pal, U. B. (2007). Effect of fuel composition on performance of single-step cofired SOFCs. *Journal of The Electrochemical Society*, 154(10), B1080.
-

Yoon, K. J., Gopalan, S., & Pal, U. B. (2008). Effect of anode active layer on performance of single step co-fired solid oxide fuel cells (SOFCs). *ECS Transactions*, 13(26), 249.

Yoon, K. J., Ye, G., Gopalan, S., & Pal, U. B. (2010). Cost-effective single step cofiring process for manufacturing solid oxide fuel cells using HSC™ anode. *Journal of Fuel Cell Science and Technology*, 7(2).

Zhao, C., Liu, R., Wang, S., Wang, Z., Qian, J., & Wen, T. (2009). Fabrication and characterization of a cathode-supported tubular solid oxide fuel cell. *Journal of power sources*, 192(2), 552-555.